Modeling and Control of Permanent-Magnet Synchronous Generators Under Open-Switch Converter Faults

Christoph M. Hackl, *Senior Member, IEEE*, Urs Pecha, and Korbinian Schechner

***Abstract*—The mathematical modeling of open-switch faults in two-level machine-side converters and the fault-tolerant current control of isotropic permanent-magnet synchronous generators are discussed in this paper. The proposed converter model is generic for any open-switch fault and independent of the operation mode of the electrical machine. The proposed fault-tolerant current control system gives improved control performance and reduced torque ripple under open-switch faults by modifying the antiwindup strategy, adapting the space-vector modulation scheme, and by injecting additional reference currents. The theoretical derivations of model and control are validated by comparative simulation and measurement results.**

***Index Terms*—Antiwindup (AW), current control, *d*-current injection, fault tolerance, field-oriented control (FOC), flat-top modulation, open-switch fault, permanent-magnet synchronous generator (PMSG), wind turbine systems.**

Notation: $\mathbb{N}, \mathbb{R}$: natural and real numbers. $\boldsymbol{x} := (x_1, \ldots, x_n)^\top \in \mathbb{R}^n$: column vector, $n \in \mathbb{N}$ where "$\top$" and ":=" mean "transposed" and "is defined as." $\boldsymbol{I}_n := \mathrm{diag}(1, \ldots, 1) \in \mathbb{R}^{n \times n}$: identity matrix. $\boldsymbol{O}_{n \times p} \in \mathbb{R}^{n \times p}$: zero matrix, $n, p \in \mathbb{N}$. $\boldsymbol{x} \in \mathbb{R}^n$ (in X)^n: physical quantity $\boldsymbol{x}$ where each of the n elements has SI unit X. $\mathrm{mod}\ (x, y)$: remainder of the division x/y, $x \in \mathbb{R}$, $y \in \mathbb{R} \backslash \{0\}$. atan2: $\mathbb{R}^2 \to [-\pi, \pi)$, $(x, y) \to \mathrm{atan2}(y, x)$: extension of the inverse tangent function to whole circle. $\boldsymbol{T}_\mathrm{c} := \frac{2}{3}\begin{bmatrix} 1 & -\frac{1}{2} & -\frac{1}{2} \\ 0 & \frac{\sqrt{3}}{2} & -\frac{\sqrt{3}}{2} \end{bmatrix}$ and $\boldsymbol{T}_\mathrm{c}^{-1} := \frac{3}{2}\begin{bmatrix} \frac{2}{3} & -\frac{1}{3} & -\frac{1}{3} \\ 0 & \frac{\sqrt{3}}{3} & -\frac{\sqrt{3}}{3} \end{bmatrix}^\top$: Clarke transformation matrix and its inverse. $\boldsymbol{T}_\mathrm{p}(\phi) := \begin{bmatrix} \cos(\phi) & -\sin(\phi) \\ \sin(\phi) & \cos(\phi) \end{bmatrix} =: \boldsymbol{T}_\mathrm{p}(-\phi)^{-1}$: Park transformation matrix. $\boldsymbol{J} = \begin{bmatrix} 0 & -1 \\ 1 & 0 \end{bmatrix}$: rotation matrix.

Manuscript received February 1, 2018; revised May 28, 2018; accepted July 2, 2018. Date of publication July 11, 2018; date of current version February 5, 2019. This work was supported by the Bavarian Ministry for Education, Culture, Science, and Art and the Munich University of Applied Sciences (MUAS) in the framework of its Open Access Publishing Program. Recommended for publication by Associate Editor J. Zhang. All authors contributed equally to this work. *(Corresponding author: Christoph M. Hackl.)*

C.M. Hackl is with the Munich University of Applied Sciences (MUAS), 80335 Munich, Germany, and head of the "Control of Renewable Energy Systems (CRES)" Research Group at Technical University of Munich (TUM), Germany (e-mail: christoph.hackl@hm.edu).

U. Pecha is with the Institute of Electrical Energy Conversion, University of Stuttgart, Stuttgart 70569, Germany (e-mail: urs.pecha@iew.uni-stuttgart.de).

K. Schechner is with the "Control of Renewable Energy Systems (CRES)" Research Group, Munich School of Engineering, Technical University of Munich (TUM), Garching 85748, Germany (e-mail: korbinian.schechner@tum.de).

Color versions of one or more of the figures in this paper are available online at http://ieeexplore.ieee.org.

Digital Object Identifier 10.1109/TPEL.2018.2855423

I. Introduction

OPEN-SWITCH faults in converters for electric drives have gained increasing attention in the last years. An open-switch fault can be caused by thermic cycling, driver failures, or by a rupture of the insulated-gate bipolar transistor (IGBT) that is induced by a short-circuit fault [1]. Unlike a short-circuit fault, an open-switch fault does usually not trigger a system shutdown, but degrades the system performance and can cause—without proper counteractions—secondary faults in other components (see [2] and [3]). Open-switch faults are therefore a crucial kind of faults in converters and should be considered in the design of a robust and fault-tolerant (hence more reliable) electrical drive system.

This far, especially, the detection of faults in the converter and the identification of the faulty switch have been the focus of research. Various detection methods have already been presented [1]–[9]. Therefore, fault detection is *not* the topic of this paper.

The focus of this paper is on a fault-tolerant modification of the control system such that, even in the presence of an open-switch fault in the machine-side converter, a continuous operation of the turbine is feasible. This is of particular interest for offshore wind turbine systems, where maintenance is expensive and depends on the weather conditions (e.g., whether ship can access the turbine or not). With a fault-tolerant control system (as proposed in this paper), the wind turbine can still be used until regular maintenance is planned or weather conditions are good. So, instead of having to shut down the generator and producing no electricity at all, the turbine can still be operated and will contribute to energy production reducing the financial loss. Without adequate fault-tolerant modifications, the faulty converter will cause increased losses and large torque ripples/oscillations, which will harm the mechanical components and the generator of the wind turbine [10].

To analyze the impact of open-switch faults, a model of the faulty converter has been proposed in [11]–[13]. The model determines the phase voltages of the electric machine connected to the faulty converter by using so-called *pole voltages* of the converter. If there is an open-switch fault in one of the switching

devices, a deviation in the pole voltage of the respective phase occurs, which affects all three phase voltages. The pole voltages are, however, a rather unintuitive quantity compared to, for example, the *switching state* of the power electronic devices or the *phase voltages* of the machine. Moreover, the use of pole voltages in simulations makes the converter model unnecessarily complicated.

To ensure a safe and uninterrupted operation of the electrical drive, a fault-tolerant control strategy has to be implemented. In [14]–[17], a modified space-vector modulation (SVM) is proposed for two-level converters. These contributions adapt the switching patterns and replace those space vectors that cannot be applied due to the open-switch fault. However, these papers do neither consider optimal phase shift angles between applied voltage and current vector nor adapt their current controllers to the postfault operation, although—as will be shown later—these measures additionally and significantly improve the overall control performance.

For three-level converters using neutral-point clamped (NPC) or T-type configurations, the redundancy in the switching states can be used to compensate for the infeasible switching states and to generate the desired voltage output nevertheless, see [4], [6], [18], and [19]. In addition, Lee and Lee [19] propose to inject an additional d-axis current to shift the phase angle between reference voltage and current to 0° if an open-switch fault occurs in one of the outer switches. This helps to avoid infeasible switching states, and therefore reduces the current distortion in the faulty phase of the generator. However, the use of redundant switching vectors cannot be used for two-level converters, since there is no sufficient redundancy in the available switching states. The impact of an open-switch fault reduces the feasible voltage area in the voltage hexagon of a two-level converter significantly. Moreover, in [4], [6], [18], and [19], the current control system and its impact on the control performance during faults are not discussed in detail.

Freire [20] proposes to consider converters with open-switch faults as *three-switch three-phase rectifiers* (all upper or lower switches are assumed to be simply diodes). It investigates the possible avoidance of infeasible zero switching vectors in SVM. To achieve a minimal current distortion, a phase shift of 180° between current and voltage vector is proposed. This phase shift is achieved by injecting an appropriate d-current. Further investigations in this paper will show that, for the considered permanent-magnet synchronous generator (PMSG), 180° is not the *optimal* phase shift angle to guarantee a minimal current distortion. Moreover, in [20], the impact of the open-switch fault on the control performance of the current controller (such as windup effects) is neither addressed nor tackled, and a generic converter model covering open-switch faults, for example, simulation purposes is not provided.

Another possibility to ensure a continued operation of the generator is the use of fault-tolerant converter configurations. Different topologies and methods to control faulty converters are described in [20]–[23]. For example, in case of open-switch faults, a fourth inverter leg can be used, or the neutral point of the machine can be connected to the midpoint of the dc bus. Both solutions can compensate for the loss of the phase with the faulty switch. However, additional and costly hardware components or reconfigurations are required in contrast to standard converter configurations.

In this paper, a fault-tolerant current control system for PMSG-based wind turbine systems is proposed where the machine-side two-level converter exhibits open-switch faults. The proposed control system does *not* require any hardware modifications and is easy to implement, since the required extensions to the standard control system are straightforward and noncomplex. Furthermore, a generic mathematical (phase) model of the faulty converter is proposed. The model relies on the *switching states* of the upper (or lower) switches and determines the phase voltages of the generator depending on the sign (direction) of the current in the faulty phase. Therefore, this model can be implemented quickly and efficiently. It is simple and easy to understand and allows very precise simulations, which give almost identical results as the conducted experiments in the laboratory. Based on this precise but simple model, the impacts of the open-switch fault on the current control performance of a standard field-oriented control (FOC) system are analyzed and a fault-tolerant control system is proposed. The proposed control system combines different modifications such as follows:

1) an improved antiwindup (AW) strategy;
2) a modified SVM;
3) an optimal d-axis current reference bringing the phase angle between voltage and current in the generator to an optimal value (which is neither 180° nor 0° for the considered machine).

All modifications and their positive effects on the control performance under open-switch faults are discussed in detail. The effectiveness of the proposed modifications is finally illustrated and validated by comparative simulation and measurement results. Concluding, with the proposed fault-tolerant approach, a continuous operation of the wind turbine system is feasible even in the faulty case while the performance degradation of the electrical drive system is rather small. Torque ripples and losses are all within an acceptable range.

II. Modeling

In this section, the models of PMSG and machine-side inverter/converter with open-switch faults are introduced. The models are derived in the three-phase (a, b, c)-reference frame.

A. Model of PMSG

The three-phase stator voltages of an isotropic PMSG are given by [24, Example 14.24]

$$\boldsymbol{u}_{\mathrm{s}}^{abc} = R_{\mathrm{s}}\boldsymbol{i}_{\mathrm{s}}^{abc} + \tfrac{\mathrm{d}}{\mathrm{d}t}\boldsymbol{\psi}_{\mathrm{s}}^{abc}(\boldsymbol{i}_{\mathrm{s}}^{abc}, \phi_{\mathrm{m}}) \tag{1}$$

with stator voltage (vector) $\boldsymbol{u}_{\mathrm{s}}^{abc} := (u_{\mathrm{s}}^a, u_{\mathrm{s}}^b, u_{\mathrm{s}}^c)^\top$ (in V)[3], stator resistance R_{s} (in Ω), stator current (vector) $\boldsymbol{i}_{\mathrm{s}}^{abc} := (i_{\mathrm{s}}^a, i_{\mathrm{s}}^b, i_{\mathrm{s}}^c)^\top$ (in A)[3], and stator flux linkage (vector) $\boldsymbol{\psi}_{\mathrm{s}}^{abc} := (\psi_{\mathrm{s}}^a, \psi_{\mathrm{s}}^b, \psi_{\mathrm{s}}^c)^\top$ (in V s)[3]. Note that the stator phase currents sum up to zero (i.e., $i_{\mathrm{s}}^a + i_{\mathrm{s}}^b + i_{\mathrm{s}}^c = 0$) due to the star connection of

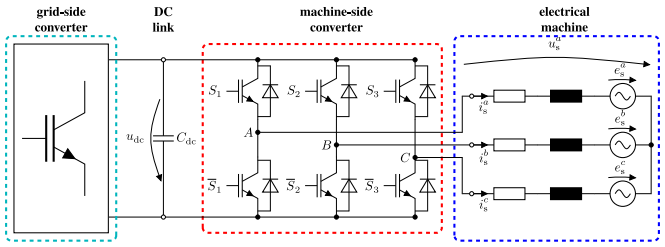

Fig. 1. Back-to-back converter with PMSG.

the stator windings. The stator flux linkage

$$\boldsymbol{\psi}_{\mathrm{s}}^{abc}(\boldsymbol{i}_{\mathrm{s}}^{abc},\phi_{\mathrm{m}})=\underbrace{\begin{bmatrix} L_{\mathrm{s,m}}+L_{\mathrm{s},\sigma} & -\frac{L_{\mathrm{s,m}}}{2} & -\frac{L_{\mathrm{s,m}}}{2} \\ -\frac{L_{\mathrm{s,m}}}{2} & L_{\mathrm{s,m}}+L_{\mathrm{s},\sigma} & -\frac{L_{\mathrm{s,m}}}{2} \\ -\frac{L_{\mathrm{s,m}}}{2} & -\frac{L_{\mathrm{s,m}}}{2} & L_{\mathrm{s,m}}+L_{\mathrm{s},\sigma} \end{bmatrix}}_{=:\boldsymbol{L}_{\mathrm{s}}^{abc}} \boldsymbol{i}_{\mathrm{s}}^{abc} + \underbrace{\hat{\psi}_{\mathrm{pm}} \begin{pmatrix} \cos\left(n_{\mathrm{p}}\left(\phi_{\mathrm{m}}+\phi_{\mathrm{pm}}\right)\right) \\ \cos\left(n_{\mathrm{p}}\left(\phi_{\mathrm{m}}+\phi_{\mathrm{pm}}\right)-\frac{2}{3}\pi\right) \\ \cos\left(n_{\mathrm{p}}\left(\phi_{\mathrm{m}}+\phi_{\mathrm{pm}}\right)-\frac{4}{3}\pi\right) \end{pmatrix}}_{=:\boldsymbol{\psi}_{\mathrm{pm}}^{abc}(\phi_{\mathrm{m}})} \tag{2}$$

depends on the inductance matrix $\boldsymbol{L}_{\mathrm{s}}^{abc}$ (in $\frac{\mathrm{Vs}}{\mathrm{A}}$)[3] with stator main inductance $L_{\mathrm{s,m}}$ and stator leakage inductance $L_{\mathrm{s},\sigma}$ (both in $\frac{\mathrm{Vs}}{\mathrm{A}}$), stator currents $\boldsymbol{i}_{\mathrm{s}}^{abc}$ and permanent magnet (PM) flux linkage vector $\boldsymbol{\psi}_{\mathrm{pm}}^{abc}$ with PM-flux linkage amplitude $\hat{\psi}_{\mathrm{pm}}$ (in V s), number n_{p} of pole pairs, machine (mechanical) angle $\phi_{\mathrm{m}}:=\int\omega_{\mathrm{m}}(\tau)d\tau$ (in rad), and (initial) angle ϕ_{pm} (in rad) of the PM. Inserting (2) into (1) yields the current dynamics combined with the mechanical dynamics in the (a,b,c)-reference frame (see Fig. 1) as follows:

$$\left.\begin{aligned} \tfrac{\mathrm{d}}{\mathrm{d}t}\boldsymbol{i}_{\mathrm{s}}^{abc}(t) &= (\boldsymbol{L}_{\mathrm{s}}^{abc})^{-1}\Bigg[\boldsymbol{u}_{\mathrm{s}}^{abc}(t)-R_{\mathrm{s}}\boldsymbol{i}_{\mathrm{s}}^{abc}(t) \\ &\quad \underbrace{+n_{\mathrm{p}}\omega_{\mathrm{m}}(t)\hat{\psi}_{\mathrm{pm}}\begin{pmatrix} \sin\left(n_{\mathrm{p}}\left(\phi_{\mathrm{m}}(t)+\phi_{\mathrm{pm}}\right)\right) \\ \sin\left(n_{\mathrm{p}}\left(\phi_{\mathrm{m}}(t)+\phi_{\mathrm{pm}}\right)-\frac{2}{3}\pi\right) \\ \sin\left(n_{\mathrm{p}}\left(\phi_{\mathrm{m}}(t)+\phi_{\mathrm{pm}}\right)-\frac{4}{3}\pi\right) \end{pmatrix}}_{=:-\boldsymbol{e}_{\mathrm{s}}^{abc}=-(e_{\mathrm{s}}^{a},e_{\mathrm{s}}^{b},e_{\mathrm{s}}^{c})^{\top}}\Bigg] \\ \tfrac{\mathrm{d}}{\mathrm{d}t}\omega_{\mathrm{m}}(t) &= \tfrac{1}{\Theta}\left(m_{\mathrm{m}}\left(\boldsymbol{i}_{\mathrm{s}}^{abc}(t),\phi_{\mathrm{m}}(t)\right)+m_{\mathrm{t}}(t)\right) \\ \tfrac{\mathrm{d}}{\mathrm{d}t}\phi_{\mathrm{m}}(t) &= \omega_{\mathrm{m}}(t) \end{aligned}\right\} \tag{3}$$

with initial currents $\boldsymbol{i}_{\mathrm{s}}^{abc}(0)=\boldsymbol{i}_{\mathrm{s},0}^{abc}$ (in A)[3], initial angular velocity $\omega_{\mathrm{m}}(0)=\omega_{\mathrm{m},0}$ (in $\frac{\mathrm{rad}}{\mathrm{s}}$), initial machine angle $\phi_{\mathrm{m}}(0)=\phi_{\mathrm{m},0}$ (in rad), induced back electromotive force voltage vector $\boldsymbol{e}_{\mathrm{s}}^{abc}=(e_{\mathrm{s}}^{a},e_{\mathrm{s}}^{b},e_{\mathrm{s}}^{c})^{\top}$ (in V)[3], total inertia Θ (in kgm^2) of the drive train, machine torque m_{m}, and turbine torque m_{t} (both in N·m). The machine torque m_{m} can be computed as follows [24, Example 14.24]:

$$m_{\mathrm{m}}(\boldsymbol{i}_{\mathrm{s}}^{abc},\phi_{\mathrm{m}})=\tfrac{n_{\mathrm{p}}}{3}(\boldsymbol{i}_{\mathrm{s}}^{abc})^{\top}\begin{bmatrix} 1 & 1-\sqrt{3} & 1+\sqrt{3} \\ 1+\sqrt{3} & 1 & 1-\sqrt{3} \\ 1-\sqrt{3} & 1+\sqrt{3} & 1 \end{bmatrix}$$

$$\begin{aligned} &\boldsymbol{\psi}_{\mathrm{s}}^{abc}(\boldsymbol{i}_{\mathrm{s}}^{abc},\phi_{\mathrm{m}}) \\ &\quad=-n_{\mathrm{p}}\hat{\psi}_{\mathrm{pm}}\begin{pmatrix} i_{\mathrm{s}}^{a}\,\sin\left(n_{\mathrm{p}}\left(\phi_{\mathrm{m}}(t)+\phi_{\mathrm{pm}}\right)\right) \\ i_{\mathrm{s}}^{b}\,\sin\left(n_{\mathrm{p}}\left(\phi_{\mathrm{m}}(t)+\phi_{\mathrm{pm}}\right)-\frac{2}{3}\pi\right) \\ i_{\mathrm{s}}^{c}\,\sin\left(n_{\mathrm{p}}\left(\phi_{\mathrm{m}}(t)+\phi_{\mathrm{pm}}\right)-\frac{4}{3}\pi\right) \end{pmatrix}. \end{aligned} \tag{4}$$

Remark II.1 (Field orientation): Aligning the synchronously rotating (d,q)-reference frame with the PM-flux linkage, i.e., applying the Clarke and Park transformation $\boldsymbol{x}^{k}=\boldsymbol{T}_{\mathrm{p}}(\phi_k)^{-1}\boldsymbol{T}_{\mathrm{c}}\boldsymbol{x}^{abc}$ with $\phi_k=\int\omega_k+\phi_{\mathrm{pm}}$ and $\omega_k=n_{\mathrm{p}}\omega_{\mathrm{m}}$ to (3) and machine torque (4) yields the machine dynamics

$$\left.\begin{aligned} \tfrac{\mathrm{d}}{\mathrm{d}t}\boldsymbol{i}_{\mathrm{s}}^{k}(t) &= \tfrac{1}{L_{\mathrm{s}}}\Bigg[\boldsymbol{u}_{\mathrm{s}}^{k}(t)-R_{\mathrm{s}}\boldsymbol{i}_{\mathrm{s}}^{k}(t)-\omega_k(t)L_{\mathrm{s}}\boldsymbol{J}\boldsymbol{i}_{\mathrm{s}}^{k}(t) \\ &\qquad -\omega_k(t)\hat{\psi}_{\mathrm{pm}}\begin{pmatrix}0\\1\end{pmatrix}\Bigg] \\ \tfrac{\mathrm{d}}{\mathrm{d}t}\omega_{\mathrm{m}}(t) &= \tfrac{1}{\Theta}\left(m_{\mathrm{m}}\left(\boldsymbol{i}_{\mathrm{s}}^{k}(t)\right)+m_{\mathrm{t}}(t)\right) \\ \tfrac{\mathrm{d}}{\mathrm{d}t}\phi_{\mathrm{m}}(t) &= \omega_{\mathrm{m}}(t) \end{aligned}\right\} \tag{5}$$

with initial values $\boldsymbol{i}_{\mathrm{s}}^{k}(0)=\boldsymbol{T}_{\mathrm{p}}^{-1}(\phi_k(0))\boldsymbol{T}_{\mathrm{c}}\boldsymbol{i}_{\mathrm{s},0}^{abc}$, $\omega_{\mathrm{m}}(0)=\omega_{\mathrm{m},0}$, and $\phi_{\mathrm{m}}(0)=\phi_{\mathrm{m},0}$ in the *PM-flux linkage orientation* (or, simply, *field orientation*; see, e.g., [24, Ch. 14] or [25, Sec. 3.2.2]) with stator voltages $\boldsymbol{u}_{\mathrm{s}}^{k}:=(u_{\mathrm{s}}^{d},\,u_{\mathrm{s}}^{q})^{\top}$ (in V)[2], stator currents $\boldsymbol{i}_{\mathrm{s}}^{k}:=(i_{\mathrm{s}}^{d},\,i_{\mathrm{s}}^{q})$ (in A)[2], stator inductance $L_{\mathrm{s}}:=\frac{3}{2}L_{\mathrm{s,m}}+L_{\mathrm{s},\sigma}$ (in $\frac{\mathrm{Vs}}{\mathrm{A}}$) and flux linkage $\boldsymbol{\psi}_{\mathrm{s}}^{k}:=(\psi_{\mathrm{s}}^{d},\,\psi_{\mathrm{s}}^{q})^{\top}$ (in V s)[2], and the machine torque

$$m_{\mathrm{m}}(\boldsymbol{i}_{\mathrm{s}}^{k})=\tfrac{3}{2}n_{\mathrm{p}}(\boldsymbol{i}_{\mathrm{s}}^{k})^{\top}\boldsymbol{J}\boldsymbol{\psi}_{\mathrm{s}}^{k}=\tfrac{3}{2}n_{\mathrm{p}}\hat{\psi}_{\mathrm{pm}}i_{\mathrm{s}}^{q}. \tag{6}$$

B. Model of Converter

1) Model of Converter Without Faults: Fig. 1 shows a back-to-back converter with PMSG. The output voltage of the machine-side converter is the stator voltage, given by [26]

$$\boldsymbol{u}_{\mathrm{s}}^{abc}(u_{\mathrm{dc}},\boldsymbol{s}_{\mathrm{s}}^{abc})=\tfrac{u_{\mathrm{dc}}}{3}\begin{bmatrix} 2 & -1 & -1 \\ -1 & 2 & -1 \\ -1 & -1 & 2 \end{bmatrix}\boldsymbol{s}_{\mathrm{s}}^{abc} \tag{7}$$

and depends in the fault-free case for a star-connected, symmetrical electrical machine only on the actual switching vector $\boldsymbol{s}_{\mathrm{s}}^{abc}=(s_{\mathrm{s}}^{a},\,s_{\mathrm{s}}^{b},\,s_{\mathrm{s}}^{c})^{\top}$ and the actual dc-link voltage u_{dc} (in V). A "1" in the switching vector $\boldsymbol{s}_{\mathrm{s}}^{abc}$ means that the upper switch is closed. A "0" represents a closed lower switch. For example, a switching vector $\boldsymbol{s}_{\mathrm{s}}^{abc}=(1,\,1,\,0)^{\top}$ yields the closed switches S_1, S_2, and $\overline{S}_3$ (S_3 is open). Applying the Clarke transformation to (7) allows to transform $\boldsymbol{u}_{\mathrm{s}}^{abc}$ to

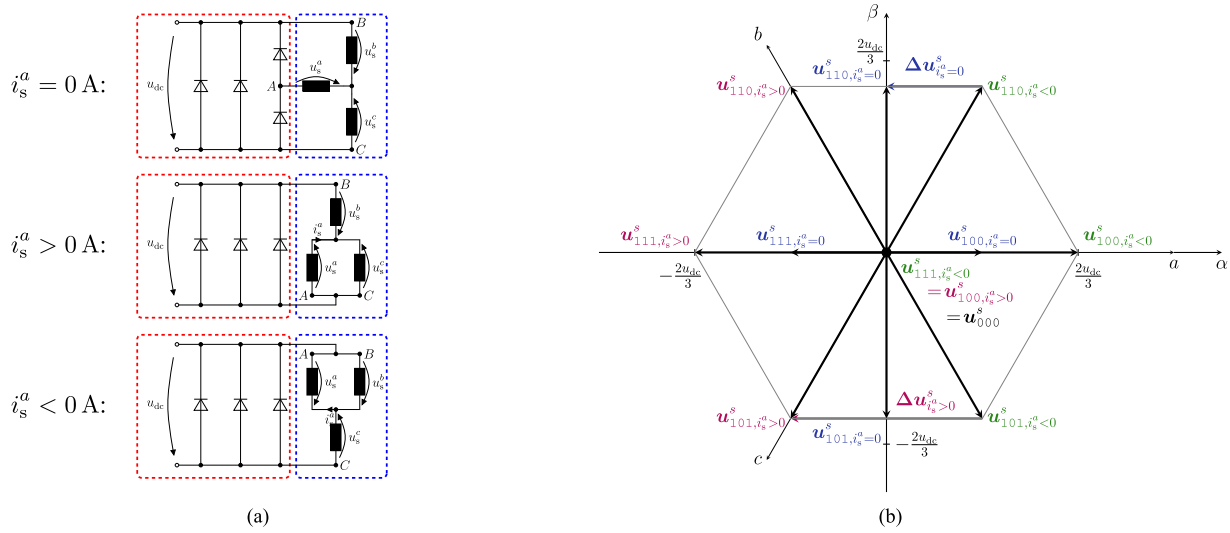

Fig. 2. Illustration of impact of open-switch fault in S_1 on (a) electrical equivalent circuit of machine-side converter and PMSG for $\boldsymbol{s}_\mathrm{s}^{abc} = (1,\,1,\,0)^\top$ (for simplicity, the windings are shown as inductances) and (b) voltage hexagon with *shifted* shifted voltage vectors $\boldsymbol{u}_\mathrm{s}^s$ for $i_\mathrm{s}^a = 0$, $i_\mathrm{s}^a > 0$, and all possible $\boldsymbol{s}_\mathrm{s}^{abc}$.

the two-dimensional stator fixed (α,β)-reference frame as follows $\boldsymbol{u}_\mathrm{s}^s := \left(u_\mathrm{s}^\alpha,\, u_\mathrm{s}^\beta\right)^\top = \boldsymbol{T}_c \boldsymbol{u}_\mathrm{s}^{abc}$.

2) Model of Converter With One Open-Switch Fault: At first, the model is derived for an open-switch fault in S_1. Afterward, the generalization of the faulty converter model is presented. Without loss of generality, the open-switch fault is assumed to appear in switch S_1. Hence, switch S_1 is always open independent of the switching vector $\boldsymbol{s}_\mathrm{s}^{abc}$ of the converter. With this fault present, the voltage $\boldsymbol{u}_\mathrm{s}^{abc}$ does not solely depend on the dc-link voltage u_dc and the switching vector $\boldsymbol{s}_\mathrm{s}^{abc}$, but also on the sign (direction) of the current i_s^a in phase a. Fig. 2(a) illustrates the different connection possibilities of the windings of the electrical machine taking the sign of the current into account and whether the free-wheeling diode of S_1 is conducting or not (compare also with Fig. 1). The resulting (shifted) voltage hexagon for this case is shown in Fig. 2(b). The following observations can be made.

1) For $i_\mathrm{s}^a = 0$, the voltage vectors (see blue symbols) with a "1" for S_1 are shifted by $\boldsymbol{\Delta u}^s_{i_\mathrm{s}^a=0} = -\frac{1}{3}u_\mathrm{dc}$ in negative a-direction [see, e.g., $\boldsymbol{u}^s_{\mathtt{110},i_\mathrm{s}^a=0}$ or $\boldsymbol{u}^s_{\mathtt{101},i_\mathrm{s}^a=0}$ in Fig. 2(b)]. Normal operation is *not* feasible.
2) For $i_\mathrm{s}^a > 0$, the voltage vectors (see magenta symbols) with a "1" for S_1 are shifted by $\boldsymbol{\Delta u}^s_{i_\mathrm{s}^a>0} = -\frac{2}{3}u_\mathrm{dc}$ in negative a-direction [see, e.g., $\boldsymbol{u}_{\,\mathtt{110}}, i_\mathrm{s}^a > 0^s$ or $\boldsymbol{u}^s_{\mathtt{101},i_\mathrm{s}^a>0}$ in Fig. 2(b)]. Normal operation is *not* feasible.
3) For $i_\mathrm{s}^a < 0$, the voltage vectors (see green symbols) are *not* shifted [see, e.g., $\boldsymbol{u}^s_{\mathtt{101},i_\mathrm{s}^a<0}$ or $\boldsymbol{u}^s_{\mathtt{110},i_\mathrm{s}^a<0}$ in Fig. 2(b)]. Normal operation is feasible.

In Fig. 3, the feasible voltage areas in the voltage hexagon and the feasible voltage vectors $\boldsymbol{u}_\mathrm{s}^s$ for open-switch faults in S_1 are shown depending on the direction of current i_s^a. For $i_\mathrm{s}^a < 0$, the full voltage hexagon can be used. For $i_\mathrm{s}^a = 0$ or $i_\mathrm{s}^a > 0$, the feasible areas in the voltage hexagon become smaller. Most critical case occurs for $i_\mathrm{s}^a > 0$, where only the sectors III and IV are feasible. Combining the observations above, the converter model (7) must be extended for an open-switch fault in S_1

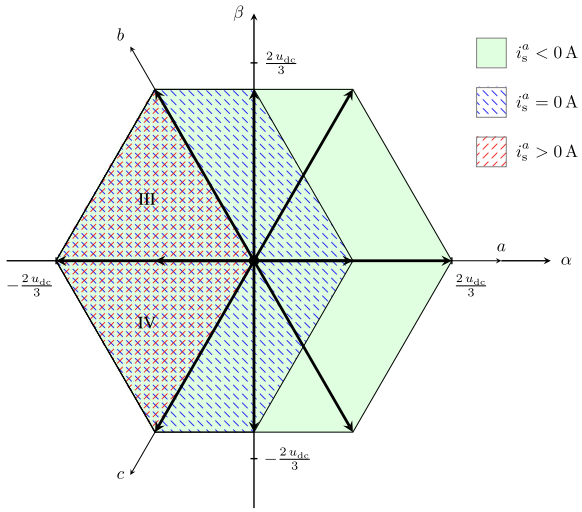

Fig. 3. Voltage hexagon with feasible sectors and voltage vectors under open-switch fault in S_1 depending on current i_s^a.

as follows:

$$\boldsymbol{u}_\mathrm{s}^{abc} = \underbrace{\frac{u_\mathrm{dc}}{3}\left(\begin{bmatrix} 2 & -1 & -1 \\ -1 & 2 & -1 \\ -1 & -1 & 2 \end{bmatrix} + \begin{cases} \boldsymbol{O}_{3\times3}, & \text{if } i_\mathrm{s}^a < 0\,\mathrm{A} \\ \begin{bmatrix} -1 & 0 & 0 \\ \frac{1}{2} & 0 & 0 \\ \frac{1}{2} & 0 & 0 \end{bmatrix}, & \text{if } i_\mathrm{s}^a = 0\,\mathrm{A} \\ \begin{bmatrix} -2 & 0 & 0 \\ 1 & 0 & 0 \\ 1 & 0 & 0 \end{bmatrix}, & \text{if } i_\mathrm{s}^a > 0\,\mathrm{A} \end{cases}\right)}_{=:\boldsymbol{S}_{S_1}(i_\mathrm{s}^a)} \boldsymbol{s}_\mathrm{s}^{abc}. \tag{8}$$

The switching matrix $\boldsymbol{S}_{S_1}(i_\mathrm{s}^a) \in \mathbb{R}^{3\times3}$ exclusively models the converter for an open-switch fault in S_1 and changes with the

TABLE I
COMPLETE MODEL OF A FAULTY CONVERTER WITH SWITCHING MATRICES $\boldsymbol{S}_y$ AND $\boldsymbol{S}_z$ FOR FAULTY SWITCHES S_1, S_2, S_3, AND $\overline{S}_1, \overline{S}_2, \overline{S}_3$, RESPECTIVELY

Converter output phase voltage $\boldsymbol{u}_{\mathrm{s}}^{abc} = \frac{u_{\mathrm{dc}}}{3}\boldsymbol{S}_y(i_{\mathrm{s}}^x)\,\boldsymbol{s}_{\mathrm{s}}^{abc}$ for faults in the *upper* switches

	$y = S_1, x = a$	$y = S_2, x = b$	$y = S_3, x = c$
$\boldsymbol{S}_y(i_{\mathrm{s}}^x < 0\,\mathrm{A})$	$\begin{bmatrix} 2 & -1 & -1 \\ -1 & 2 & -1 \\ -1 & -1 & 2 \end{bmatrix}$	$\begin{bmatrix} 2 & -1 & -1 \\ -1 & 2 & -1 \\ -1 & -1 & 2 \end{bmatrix}$	$\begin{bmatrix} 2 & -1 & -1 \\ -1 & 2 & -1 \\ -1 & -1 & 2 \end{bmatrix}$
$\boldsymbol{S}_y(i_{\mathrm{s}}^x = 0\,\mathrm{A})$	$\begin{bmatrix} 1 & -1 & -1 \\ -\frac{1}{2} & 2 & -1 \\ -\frac{1}{2} & -1 & 2 \end{bmatrix}$	$\begin{bmatrix} 2 & -\frac{1}{2} & -1 \\ -1 & 1 & -1 \\ -1 & -\frac{1}{2} & 2 \end{bmatrix}$	$\begin{bmatrix} 2 & -1 & -\frac{1}{2} \\ -1 & 2 & -\frac{1}{2} \\ -1 & -1 & 1 \end{bmatrix}$
$\boldsymbol{S}_y(i_{\mathrm{s}}^x > 0\,\mathrm{A})$	$\begin{bmatrix} 0 & -1 & -1 \\ 0 & 2 & -1 \\ 0 & -1 & 2 \end{bmatrix}$	$\begin{bmatrix} 2 & 0 & -1 \\ -1 & 0 & -1 \\ -1 & 0 & 2 \end{bmatrix}$	$\begin{bmatrix} 2 & -1 & 0 \\ -1 & 2 & 0 \\ -1 & -1 & 0 \end{bmatrix}$

Converter output phase voltage $\boldsymbol{u}_{\mathrm{s}}^{abc} = \frac{u_{\mathrm{dc}}}{3}\boldsymbol{S}_z(i_{\mathrm{s}}^x)\,\overline{\boldsymbol{s}}_{\mathrm{s}}^{abc}$ for faults in the *lower* switches

	$z = \overline{S}_1, x = a$	$z = \overline{S}_2, x = b$	$z = \overline{S}_3, x = c$
$\boldsymbol{S}_z(i_{\mathrm{s}}^x < 0\,\mathrm{A})$	$\begin{bmatrix} 0 & 1 & 1 \\ 0 & -2 & 1 \\ 0 & 1 & -2 \end{bmatrix}$	$\begin{bmatrix} -2 & 0 & 1 \\ 1 & 0 & 1 \\ 1 & 0 & -2 \end{bmatrix}$	$\begin{bmatrix} -2 & 1 & 0 \\ 1 & -2 & 0 \\ 1 & 1 & 0 \end{bmatrix}$
$\boldsymbol{S}_z(i_{\mathrm{s}}^x = 0\,\mathrm{A})$	$\begin{bmatrix} -1 & 1 & 1 \\ \frac{1}{2} & -2 & 1 \\ \frac{1}{2} & 1 & -2 \end{bmatrix}$	$\begin{bmatrix} -2 & \frac{1}{2} & 1 \\ 1 & -1 & 1 \\ 1 & \frac{1}{2} & -2 \end{bmatrix}$	$\begin{bmatrix} -2 & 1 & \frac{1}{2} \\ 1 & -2 & \frac{1}{2} \\ 1 & 1 & -1 \end{bmatrix}$
$\boldsymbol{S}_z(i_{\mathrm{s}}^x > 0\,\mathrm{A})$	$\begin{bmatrix} -2 & 1 & 1 \\ 1 & -2 & 1 \\ 1 & 1 & -2 \end{bmatrix}$	$\begin{bmatrix} -2 & 1 & 1 \\ 1 & -2 & 1 \\ 1 & 1 & -2 \end{bmatrix}$	$\begin{bmatrix} -2 & 1 & 1 \\ 1 & -2 & 1 \\ 1 & 1 & -2 \end{bmatrix}$

direction of the phase current i_{s}^a. Generalizing the observations above to an arbitrary open-switch fault in one of the six switches $S_1, S_2, S_3, \overline{S}_1, \overline{S}_2$, and $\overline{S}_3$, and introducing the negated switching vector

$$\overline{\boldsymbol{s}}_{\mathrm{s}}^{abc} := \mathbf{1}_3 - \boldsymbol{s}_{\mathrm{s}}^{abc} \text{ where } \mathbf{1}_3 := (1,\,1,\,1)^\top \tag{9}$$

leads to different switching matrices $\boldsymbol{S}_y(i_{\mathrm{s}}^x)$ and $\boldsymbol{S}_z(i_{\mathrm{s}}^x)$ with $x \in \{a, b, c\}$, $y \in \{S_1, S_2, S_3\}$, and $z \in \{\overline{S}_1, \overline{S}_2, \overline{S}_3\}$, respectively. Finally, the switching matrices for all possible faults in the six switches $S_1, S_2, S_3, \overline{S}_1, \overline{S}_2$, and $\overline{S}_3$ and the respective phase current directions are collected in Table I (details are omitted due to space limitations).

III. CURRENT CONTROL SYSTEM

Proportional-integral (PI) controllers and FOC are a common choice for the current control system in electrical drives (see [25, Sec. 3.2.2] or [27, Sec. 14.6]). In most cases, the PI controllers are equipped with an AW strategy and cross-coupling feedforward compensation terms to compensate for the cross-coupling between d- and q-currents. In this section, at first, standard FOC is briefly revisited. Afterward, the crucial modifications to improve the control performance under open-switch faults are proposed. The impact of an open-switch fault on the standard control system and the improvements achieved by the proposed fault-tolerant control system are illustrated and analyzed in simulations (see Sections III-A5 and III-B, respectively). Finally, the simulation results are validated by comparative measurement results in Section IV.

A. Standard Control System (FOC)

In Fig. 4, the block diagram of the standard control system consisting of 1) PI controllers with AW, 2) cross-coupling feedforward compensation, 3) reference voltage saturation, and

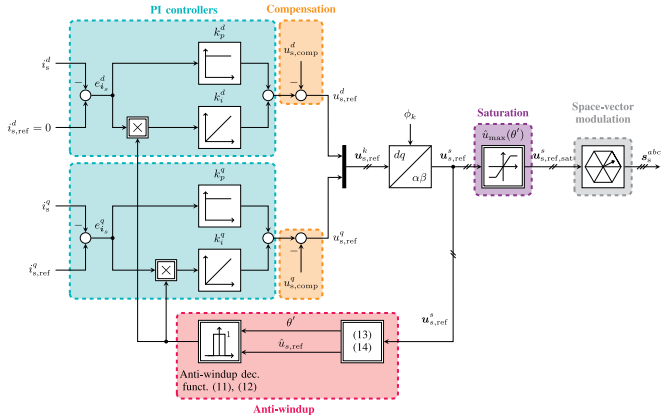

Fig. 4. Standard control system (FOC): PI controllers with AW, cross-coupling feedforward compensation, and reference voltage saturation.

4) modulation is depicted. In the following sections, each block will be explained briefly.

1) PI Controllers With AW: The PI controllers weight and integrate the current control error

$$\boldsymbol{e}_{\boldsymbol{i}_{\mathrm{s}}}^k(t) := \begin{pmatrix} e_{\boldsymbol{i}_{\mathrm{s}}}^d(t) \\ e_{\boldsymbol{i}_{\mathrm{s}}}^q(t) \end{pmatrix} := \begin{pmatrix} i_{\mathrm{s,ref}}^d(t) - i_{\mathrm{s}}^d(t) \\ i_{\mathrm{s,ref}}^q(t) - i_{\mathrm{s}}^q(t) \end{pmatrix} \tag{10}$$

defined as the difference between reference currents (coming, e.g., from outer control loops) and the actual currents. Output $\boldsymbol{u}_{\mathrm{s,PI}}^k = (u_{\mathrm{s,PI}}^d,\, u_{\mathrm{s,PI}}^q)^\top$ and dynamics of integrator $\boldsymbol{\xi}_{\mathrm{i}}^k = (\xi_{\mathrm{i}}^d,\, \xi_{\mathrm{i}}^q)^\top$ of the PI controllers with AW decision function $f_{\mathrm{aw}}(\cdot)$ are as follows:

$$\left.\begin{aligned} \boldsymbol{u}_{\mathrm{s,PI}}^k(t) &= \begin{bmatrix} k_{\mathrm{p}}^d & 0 \\ 0 & k_{\mathrm{p}}^q \end{bmatrix} \boldsymbol{e}_{\boldsymbol{i}_{\mathrm{s}}}^k(t) + \begin{bmatrix} k_{\mathrm{i}}^d & 0 \\ 0 & k_{\mathrm{i}}^q \end{bmatrix} \boldsymbol{\xi}_{\mathrm{i}}^k(t) \\ \tfrac{\mathrm{d}}{\mathrm{d}t}\boldsymbol{\xi}_{\mathrm{i}}^k(t) &= f_{\mathrm{aw}}\big(\hat{u}_{\mathrm{s,ref}}(t)\big) \cdot \boldsymbol{e}_{\boldsymbol{i}_{\mathrm{s}}}^k(t), \quad \boldsymbol{\xi}_{\mathrm{i}}^k(0) = \mathbf{0}_2 \end{aligned}\right\} \tag{11}$$

with proportional and integral controller gains k_{p}^d and k_{p}^q and k_{i}^d and k_{i}^q, respectively. For example, a model-based tuning is according to the *magnitude optimum* (see, e.g., [26]), which leads to the following controller gains $k_{\mathrm{p}}^d = k_{\mathrm{p}}^q = \frac{L_{\mathrm{s}} f_{\mathrm{sw}}}{3}$ and $k_{\mathrm{i}}^d = k_{\mathrm{i}}^q = \frac{R_{\mathrm{s}} f_{\mathrm{sw}}}{3}$, where f_{sw} (in Hz) is switching frequency of the converter/inverter. Any other reasonable tuning rule might also be applicable. The AW decision function

$$f_{\mathrm{aw}}\big(\hat{u}_{\mathrm{s,ref}}\big) := \begin{cases} 1 & \text{, if } \hat{u}_{\mathrm{s,ref}} \le \hat{u}_{\max}(u_{\mathrm{dc}}, \theta') \\ 0 & \text{, else} \end{cases} \tag{12}$$

enables or disables integration of the integral control action (i.e., conditional integration, for more details see [24, Sec. 10.4.1]), if the applied reference voltage vector amplitude $\hat{u}_{\mathrm{s,ref}}$ (in V), defined by

$$\begin{aligned} \hat{u}_{\mathrm{s,ref}} &:= \sqrt{\big(u_{\mathrm{s,ref}}^\alpha\big)^2 + \big(u_{\mathrm{s,ref}}^\beta\big)^2} \text{ where } \boldsymbol{u}_{\mathrm{s,ref}}^{\mathrm{s}} := \begin{pmatrix} u_{\mathrm{s,ref}}^\alpha \\ u_{\mathrm{s,ref}}^\beta \end{pmatrix} \\ &:= \boldsymbol{T}_{\mathrm{p}}(\phi_k)\, \underbrace{\big(\boldsymbol{u}_{\mathrm{s,PI}}^k - \boldsymbol{u}_{\mathrm{s,comp}}^k\big)}_{=:\boldsymbol{u}_{\mathrm{s,ref}}^k} \end{aligned} \tag{13}$$

exceeds the maximally available voltage amplitude $\hat{u}_{\max}$ (in V), given by

$$\hat{u}_{\max}(u_{\mathrm{dc}},\theta') := \underbrace{\frac{\sqrt{3}}{\sin(\theta')+\sqrt{3}\cos(\theta')}}_{\frac{\sqrt{3}}{2}\leq\cdot\leq 1}\cdot\frac{2}{3}u_{\mathrm{dc}} \leq \frac{2}{3}u_{\mathrm{dc}}$$

$$\text{where } \theta' := \mathrm{mod}\big(\underbrace{\mathrm{atan2}(u^{\beta}_{\mathrm{s,ref}},u^{\alpha}_{\mathrm{s,ref}})}_{=:\theta},\tfrac{\pi}{3}\big) \in \big[0,\tfrac{\pi}{3}\big) \tag{14}$$

within the full (fault-free) voltage hexagon [see Fig. 2(b)]. The maximally available amplitude $\hat{u}_{\max}$ of the converter depends on the voltage reference angle (in "°") and the dc-link voltage. Note that $\hat{u}_{\max}$ varies inside the voltage hexagon. It is larger for $\theta = 0°$ or $\theta = 60°$ (maximum voltage amplitude $\hat{u}_{\max}(u_{\mathrm{dc}},0) = \frac{2}{3}u_{\mathrm{dc}}$) than for $\theta = 30°$ (minimum voltage amplitude $\hat{u}_{\max}(u_{\mathrm{dc}},\pi/6) = \frac{1}{\sqrt{3}}u_{\mathrm{dc}}$). Invoking trigonometric identities leads to the expression of $\hat{u}_{\max}$ in (14) by only considering the first sector of the voltage hexagon, i.e., $\theta = \theta' \in [0°, 60°)$. Note that, in the first sector, θ' coincides with θ. Then, by using the auxiliary phase angle θ' as defined in (14), the generalized formula for the available amplitude $\hat{u}_{\max}$ is obtained for all other sectors of the voltage hexagon.

2) Cross-Coupling Feedforward Compensation: The compensation of cross-coupling terms in the current dynamics (5) is realized by the following feedforward control action:

$$\begin{aligned}\boldsymbol{u}^{k}_{\mathrm{s,comp}}(t) &:= \begin{pmatrix} u^{d}_{\mathrm{s,comp}}(t) \\ u^{q}_{\mathrm{s,comp}}(t)\end{pmatrix} \\ &:= -\omega_k(t)L_{\mathrm{s}}\boldsymbol{J}\boldsymbol{i}^{k}_{\mathrm{s}}(t) - \omega_k(t)\hat{\psi}_{\mathrm{pm}}\begin{pmatrix}0\\1\end{pmatrix} \\ &= \begin{pmatrix} \omega_k(t)L_{\mathrm{s}}i^{q}_{\mathrm{s}}(t) \\ -\omega_k(t)L_{\mathrm{s}}i^{d}_{\mathrm{s}}(t) - \omega_k(t)\hat{\psi}_{\mathrm{pm}}\end{pmatrix}\end{aligned} \tag{15}$$

which (at least in steady state) cancels out the influence of the q-terms on the d-current dynamics and vice versa (see (5) in Section II-A).

3) Reference Voltage Saturation: To avoid undesirable and infeasible output voltages of the converter by applying physically infeasible voltage reference vectors, the computed reference voltage vector $\boldsymbol{u}^{\mathrm{s}}_{\mathrm{s,ref}}$ as in (13) is saturated if necessary as follows:

$$\boldsymbol{u}^{\mathrm{s}}_{\mathrm{s,ref,sat}}(t) = \begin{cases} \boldsymbol{u}^{\mathrm{s}}_{\mathrm{s,ref}}(t) & \text{, if } \hat{u}_{\mathrm{s,ref}}(t) \leq \hat{u}_{\max}(t) \\ \hat{u}_{\max}(t)\begin{pmatrix}\cos\big(\theta(t)\big)\\ \sin\big(\theta(t)\big)\end{pmatrix} & \text{, else.}\end{cases} \tag{16}$$

Note that the reference voltage saturation does only alter the length of the voltage vector not its direction.

4) Space-Vector Modulation: To generate the switching sequence and, in particular, the switching vector $\boldsymbol{s}^{abc}_{\mathrm{s}}$ based on the saturated reference voltage $\boldsymbol{u}^{\mathrm{s}}_{\mathrm{s,ref,sat}}$, a symmetrical SVM is used in this paper (see [25, Sec. 2.4.1] or [27, Ch. 14]). The boundary (adjacent) space vectors of the respective sector and, usually, both zero vectors $\boldsymbol{u}_{000}$ and $\boldsymbol{u}_{111}$ are applied to approximate the reference voltage vector $\boldsymbol{u}^{\mathrm{s}}_{\mathrm{s,ref,sat}}$ over one switching period $T_{\mathrm{sw}} = 1/f_{\mathrm{sw}}$ (in s). To do so, T_{sw} is divided into three time intervals: T_1 for the first nonzero vector, T_2 for the second nonzero vector, and T_0 for the zero vectors such that $T_1 + T_2 + T_0 = T_{\mathrm{sw}}$ [see Figs. 2(b) and 6(a)]. If the voltage reference vector is not saturated [see Section III-A3], this will lead—depending on the implementation of the SVM—e.g., to a negative time for T_0, which will cause strange behavior of the SVM.

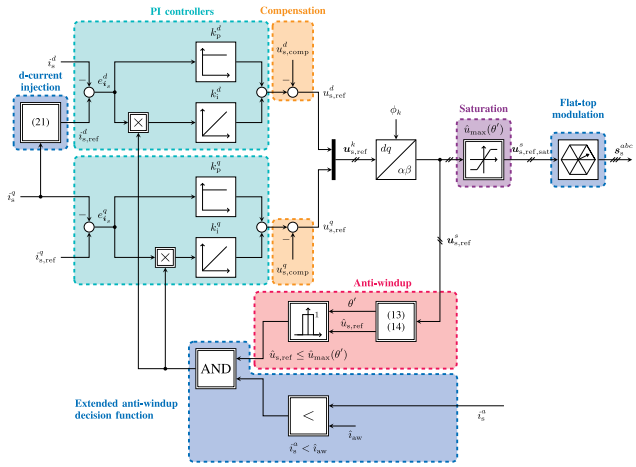

Fig. 5. Fault-tolerant control system (modified FOC; changes in blue) for an open-switch fault in S_1 (phase a): PI controllers with improved AW, cross-coupling feedforward compensation, and reference voltage saturation.

5) Control Performance of Standard Control System Under an Open-Switch Fault in S_1 (Phase a): To have a measure to evaluate the control performance of the standard and the fault-tolerant control systems, the total harmonic distortion (THD) is used. The $\mathrm{THD}_{i^a_{\mathrm{s}}}$ (in %) of, e.g., the phase current i^a_{s} can be computed as follows [28]:

$$\mathrm{THD}_{i^a_{\mathrm{s}}} := \frac{\sqrt{\sum_{n=2}^{\infty}(I^a_n)^2}}{I^a_1} \geq 0 \tag{17}$$

where I^a_1 and I^a_n (both in A) are the root-mean-square (rms) values[1] of the fundamental and the n-th harmonic current component, respectively. Fig. 10(a) shows the control performance of the standard control system [as in Fig. 4] under an open-switch fault in S_1 (phase a). The upper subplot illustrates reference ($i^d_{\mathrm{s,ref}}$ and $i^q_{\mathrm{s,ref}}$) and actual currents (i^d_{s} and i^q_{s}) in the (d,q)-reference frame, whereas the lower subplot shows the phase currents i^a_{s}, i^b_{s}, and i^c_{s} over time. It can be clearly seen that the current i^a_{s} of phase a is sinusoidal for the negative half-wave, but nonsinusoidal (close to zero) for the positive half-wave. This deviation leads to nonconstant (as usually expected) currents i^d_{s} and i^q_{s}, which significantly differ from their respective reference values $i^d_{\mathrm{s,ref}}$ and $i^q_{\mathrm{s,ref}}$ for (almost) all time. The current i^q_{s} tends to zero during the nonexisting positive half-wave of i^a_{s}. Moreover, even for the negative (correct) half-wave of i^a_{s}, the current i^q_{s} is not capable of tracking its reference $i^q_{\mathrm{s,ref}}$. In particular, the

[1]The rms value is defined by $I := \sqrt{\frac{1}{T}\int_{t-T}^{t} i(\tau)^2 d\tau}$ with fundamental period $T = 1/f$ of the current $i(\cdot)$.

nonconstant and nonlinearly oscillating evolution of i_{s}^{q} leads to noticeable torque ripples. The nonzero current i_{s}^{d} does not contribute to the torque [recall (6)] but increases copper losses in the machine. In conclusion, the standard control system performance is not acceptable and must be improved to allow for a safe and uninterrupted operation of the wind turbine system.

B. Proposed Fault-Tolerant Control System (Modified FOC)

As illustrated in Fig. 10(a), the standard control system performance is poor and not acceptable when an open-swich fault is present. Without altering the hardware or the principle control system, three (software) modifications are proposed to improve the control performance of the wind turbine system under open-switch faults in one phase. The three modifications are as follows:

1) extension of the AW strategy;
2) modification of the SVM;
3) torque ripple minimization by injecting an optimal d-current.

Each modification is explained in detail and its positive effect on the control performance of the fault-tolerant control system is illustrated by simulation results. Later, in Section IV, these modifications are implemented on a laboratory test bench and their effectiveness is validated by measurements. The block diagram of the improved and fault-tolerant control system is depicted in Fig. 5. The modifications are highlighted in blue.

1) Extension of AW Strategy: To improve the control performance under faults, in a first step, the AW strategy (12) of the PI current controllers (11) is modified. The overshoots in the q-current during the open-switch fault in S_1 [recall Fig. 10(a)] are—at least partly—due to windup of the integral control action of the PI controllers during the positive (almost zero) half-wave of i_{s}^{a}. To avoid this windup, an additional condition considering the current direction (see Fig. 5) must be introduced, which leads to the extended AW decision function

$$f_{\mathrm{aw}}^{\star}\left(\hat{u}_{\mathrm{s,ref}}, i_{\mathrm{s}}^{a}\right) := \begin{cases} 1 & \text{, if } \hat{u}_{\mathrm{s,ref}} \leq \hat{u}_{\max}(u_{\mathrm{dc}}, \theta') \\ & \quad \text{and } \; i_{\mathrm{s}}^{a} < \hat{\imath}_{\mathrm{aw}} < 0 \\ 0 & \text{, else} \end{cases} \tag{18}$$

for open-switch faults in S_1 (phase a), which replaces $f_{\mathrm{aw}}(\cdot)$ in (11). The constant $\hat{\imath}_{\mathrm{aw}} < 0$ (in A) represents the maximally admissible AW current and should be chosen negative[2] to account for the chattering of the phase current i_{s}^{a} around zero [recall Fig. 10(a)]. Note that, for any other faulty phase with open-switch fault in S_2 (or S_3), the respective phase current direction of i_{s}^{b} (or i_{s}^{c}) must be considered in (18) instead of i_{s}^{a}.

In Fig. 10(b), the improved control system performance due to the extended AW strategy (18) is shown. The abc-currents (lower subplot) do not alter much (almost no improvement is visible) and the THD reduces slightly to $\mathrm{THD}_{i_{\mathrm{s}}^{a}} = 41.4\,\%$. But the tracking performance of the currents i_{s}^{d} and, in particular, i_{s}^{q} is improved substantially. During the positive (almost zero) half-wave of i_{s}^{a}, both currents still do not perfectly track their references; but during the negative half-wave of i_{s}^{a}, both currents are capable of (almost) asymptotic reference tracking. Especially, the current ripple in the q-current is drastically reduced during the negative half-wave of i_{s}^{a}.

2) Modification of SVM (Flat-Top Modulation): The second step to improve the control performance during open-switch faults is the modification of the SVM. Note that any open-switch fault in one of the *upper* switches (i.e., S_1, S_2, or S_3) leads to a shifted zero vector $\boldsymbol{u}_{111}^{s}$ [for $i_{\mathrm{s}}^{a} \geq 0$, see Fig. 2(b)]; whereas any open-switch fault in one of the *lower* switches (i.e., $\overline{S}_1$, $\overline{S}_2$, or $\overline{S}_3$) shifts the other zero vector $\boldsymbol{u}_{000}^{s}$. Hence, one of the zero vectors is not zero any more. Then, using *flat-top* modulation allows to use only the nonshifted zero vector (see [27, Ch. 14.6] and [29]). For example, for an open-switch fault in S_1, S_2, or S_3, only the zero vector $\boldsymbol{u}_{000}^{s}$ is applied [see Fig. 6(b)]. For faults in $\overline{S}_1$, $\overline{S}_3$, or $\overline{S}_2$, only the zero vector $\boldsymbol{u}_{111}^{s}$ is used. In Fig. 10(c), the positive effect of the flat-top modulation on the control performance and the THD of i_{s}^{a} is illustrated. The upper subplots show the d- and q-currents and their references, whereas the lower subplot depicts the abc-currents for the modified control system with extended AW and modified SVM. Clearly, the intervals where $i_{\mathrm{s}}^{a} \approx 0\,\mathrm{A}$ are significantly shorter. Moreover, positive and almost sinusoidal i_{s}^{a} currents are feasible again due to the modified SVM. So, the THD value is drastically reduced to $\mathrm{THD}_{i_{\mathrm{s}}^{a}} = 19.5\,\%$ and the tracking control performances of the currents i_{s}^{d} and i_{s}^{q} are improved as well.

Remark III.1 (Small zero time): If the time T_0 of the zero vector is very small (i.e., the zero vector is applied only for a very short period of time), the proposed modification of the SVM only has a minor impact on the control performance, as the shifted zero vector is almost not used.

3) Injection of Optimal d-Current: The last improvement is to inject an optimal (additional) d-current to minimize the THD of the faulty phase even further. In the following, an open-switch fault in S_1 is considered. For other open-switch faults, the modifications are straight forward. As discussed in Section II-B2, for a fault in S_1 and $i_{\mathrm{s}}^{a} \geq 0$, the output voltages that can be provided by the faulty converter are limited. For example, $i_{\mathrm{s}}^{a} > 0$, only voltage vectors from the sectors III and IV are feasible [see Fig. 3]. The principle idea of the optimal d-current injection is to generate auxiliary reference voltage vectors within those two feasible sectors as long as possible. The goal is to determine an optimal *phase shift* φ_0 (in rad or $^\circ$) between stator current $\boldsymbol{i}_{\mathrm{s}}^{s}$ and reference voltage $\boldsymbol{u}_{\mathrm{s,ref}}^{s}$.

To illustrate the idea, in Fig. 7, the phase shifts $\varphi_0 = 150^\circ$ and $\varphi_0 = 210^\circ$ are shown for two time instants t_0 and t_1 where $\boldsymbol{i}_{\mathrm{s}}^{s}(t_0)$ and $\boldsymbol{i}_{\mathrm{s}}^{s}(t_1)$ are located on the negative and positive β-axis, respectively. Note that, if the phase current i_{s}^{a} is nonnegative, the stator current *space vector* $\boldsymbol{i}_{\mathrm{s}}^{s}$ is located in the *right* half-plane [see Fig. 7]. More precisely, at t_0 with $i_{\mathrm{s}}^{a}(t_0) = 0$ (i_{s}^{a} becomes positive thereafter), $\boldsymbol{i}_{\mathrm{s}}^{s}$ lies on the negative β-axis; whereas, at t_1 with $i_{\mathrm{s}}^{a}(t_1) = 0$ (i_{s}^{a} becomes negative afterward), $\boldsymbol{i}_{\mathrm{s}}^{s}$ is aligned with the positive β-axis. Clearly, within the interval $[t_0, t_1]$, the current moves by 180° and, optimally, the corresponding

[2] In Section IV, the threshold $\hat{\imath}_{\mathrm{aw}} = -1\,\mathrm{A}$ was chosen, which corresponds to approximately 2% of the nominal machine current [see Table II]. Clearly, this threshold depends on and has to be adjusted for the considered electrical drive system with respect to, e.g., measurement noise, sensor precision, and switching frequency of the converter.

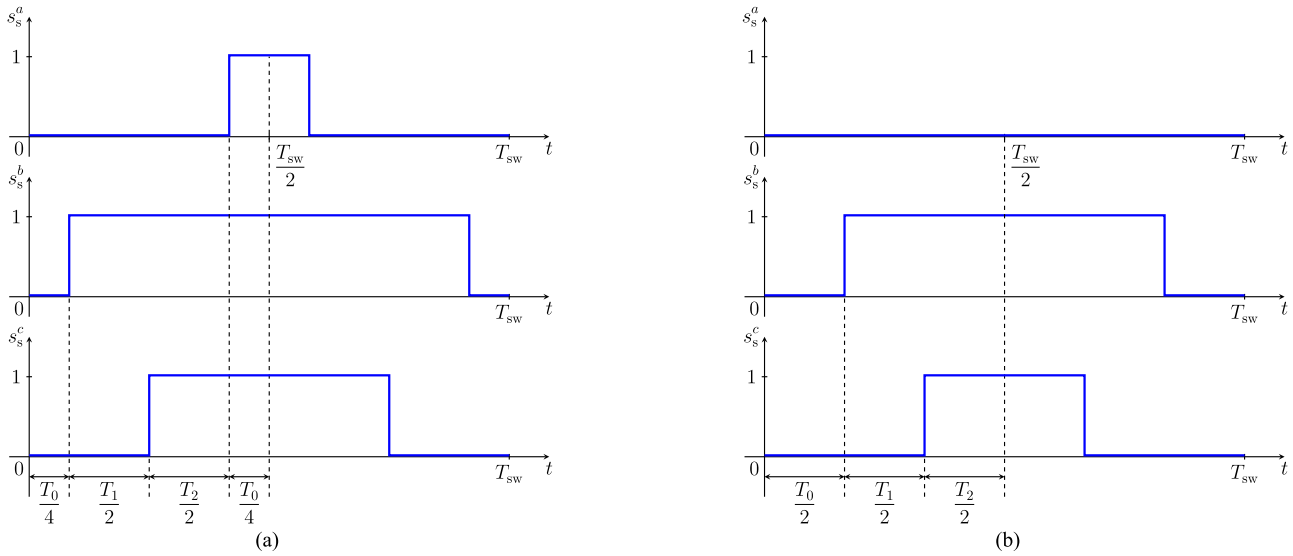

Fig. 6. Switching patterns to generate a voltage reference vector $\boldsymbol{u}^s_{s,\mathrm{ref}}$ in sector III by a linear combination of the space vectors $\boldsymbol{u}^s_{010}$, $\boldsymbol{u}^s_{011}$ and (a) standard SVM using both zero vectors $\boldsymbol{u}^s_{000}$ and $\boldsymbol{u}^s_{111}$ and (b) flat-top modulation using only the zero vector $\boldsymbol{u}^s_{000}$.

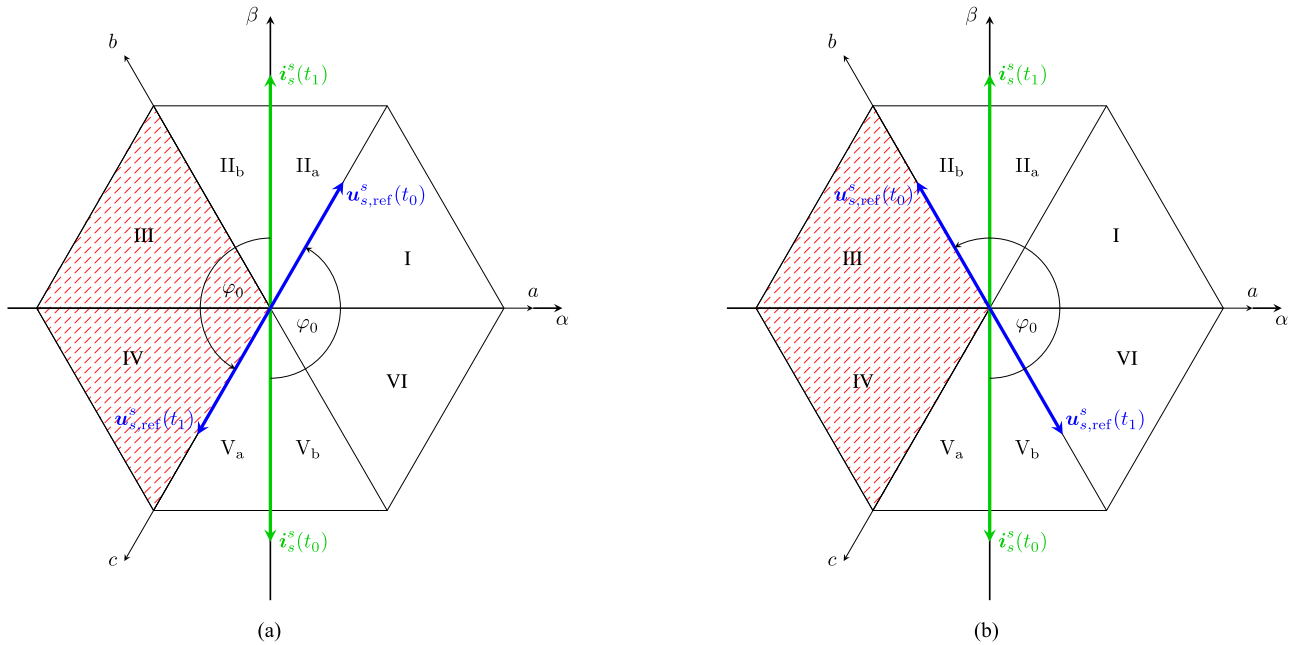

Fig. 7. Stator current vector $\boldsymbol{i}^s_{\mathrm{s}}$ and voltage reference vector $\boldsymbol{u}^s_{\mathrm{s,ref}}$ at time t_0 and t_1 for (a) $\varphi_0 = 150°$ and (b) $\varphi_0 = 210°$.

stator voltage reference *space vector* $\boldsymbol{u}^s_{\mathrm{s,ref}}$ should be within the sectors III and IV as long as possible in order to apply feasible and correct voltages to the generator. However, as these two sectors represent only span over 120°, it is not possible to apply the correct voltages during the whole nonnegative half-wave of i^a_{s} during an open-switch fault in S_1. During the remaining 60°, incorrect voltages will be applied by the faulty converter, which affect the shape of the currents and cause deviations from the desired sinusoidal waveform.

Depending on the phase shift φ_0 between stator current and reference voltage, different parts of the nonnegative half-wave of i^a_{s} are affected by the fault. For $\varphi_0 = 150°$ [see Fig. 7(a)], $\boldsymbol{u}^s_{\mathrm{s,ref}}$ starts in sector II at time t_0. So, for the first 60° of the current half-wave, incorrect voltages are applied to the generator. As soon as $\boldsymbol{u}^s_{\mathrm{s,ref}}$ enters sector III, the correct voltages can be provided (even) by the faulty converter. When $\boldsymbol{u}^s_{\mathrm{s,ref}}$ is in the sectors III and IV, the correct voltages give rise to a sinusoidal current. For $\varphi_0 = 210°$ [see Fig. 7(b)], the behavior is flipped: At time t_0, $\boldsymbol{u}^s_{\mathrm{s,ref}}$ starts already in the feasible sector III and, hence, during the first 120° of the nonnegative current half-wave, the correct voltages are applied. But, as soon as $\boldsymbol{u}^s_{\mathrm{s,ref}}$ enters sector V, incorrect voltages are generated by the converter for the rest of the half-wave until time t_1. Concluding, in order to fully benefit from the two feasible voltage sectors III and IV, where

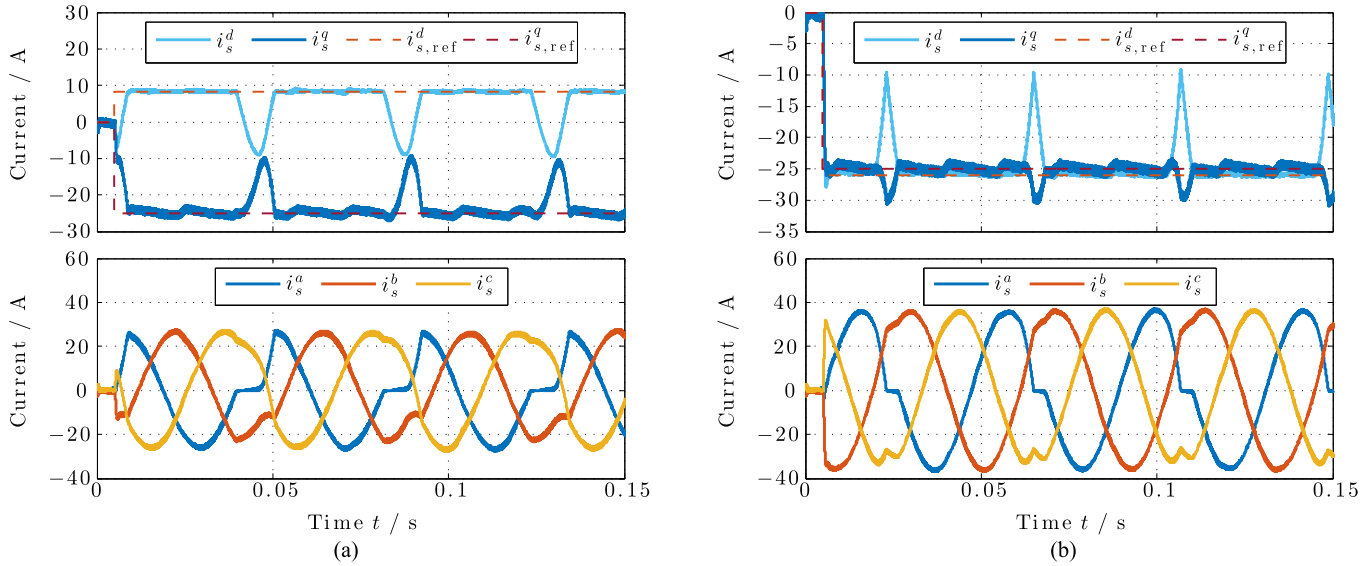

Fig. 8. Simulation results for currents $\boldsymbol{i}_{\mathrm{s}}^{k}$ (with references) and $\boldsymbol{i}_{\mathrm{s}}^{abc}$ for different phase shifts. (a) $\varphi_0 = 150^\circ$ with $\mathrm{THD}_{i_{\mathrm{s}}^a} = 31.4\,\%$. (b) $\varphi_0 = 210^\circ$ with $\mathrm{THD}_{i_{\mathrm{s}}^a} = 12.2\,\%$.

the correct voltages can be generated for $i_{\mathrm{s}}^a > 0$, the phase shift must be within the interval $\varphi_0 \in [150^\circ, 210^\circ]$. The observations above are also validated by the simulation results presented in Fig. 8: For $\varphi_0 = 150^\circ$ [see Fig. 8(a)], during the first 60°, the phase current i_{s}^a jitters around zero. In contrast to the last 120°, where the desired sinusoidal characteristic is achieved. For $\varphi_0 = 210^\circ$ [see Fig. 8(b)], the phase current i_{s}^a exhibits a sinusoidal characteristic during the first 120°, whereas, for the last 60°, it is deteriorated.

Remark III.2 (Motor mode): For a converter outputting power—e.g., for PMSGs in motor mode or for grid-side inverters in wind turbine systems, solely phase shifts of $\varphi_0 \in (-90^\circ, 90^\circ)$ are feasible. Hence, it is not possible to benefit from the sectors III and IV.

The phase shift φ_0 can be altered by the injection of a d-current, which also changes the ratio between active power p (in W) and reactive power q (in var), since (see, e.g., [26])

$$q = p\tan(\varphi_0) \quad \text{where} \quad p = \tfrac{3}{2}(\boldsymbol{u}_{\mathrm{s}}^{k})^{\top}\boldsymbol{i}_{\mathrm{s}}^{k} \quad \text{and} \quad q = \tfrac{3}{2}(\boldsymbol{u}_{\mathrm{s}}^{k})^{\top}\boldsymbol{J}\boldsymbol{i}_{\mathrm{s}}^{k}. \tag{19}$$

Moreover, note that, due to (6), i_{s}^d can be chosen independently of the desired torque. In order to derive an analytical expression for the reference current $i_{\mathrm{s,ref}}^d$ of the to-be-injected current i_{s}^d, the following assumption is imposed.

Assumption (A.1): The copper losses in the PMSG are negligible and its current dynamics are in steady state, i.e.,

$$R_{\mathrm{s}} \approx 0\,\Omega \quad \text{and} \quad \tfrac{\mathrm{d}}{\mathrm{d}t}\boldsymbol{i}_{\mathrm{s}}^{k} = \boldsymbol{0}_2. \tag{20}$$

Solving (5) (in steady state) for $\boldsymbol{u}_{\mathrm{s}}^{k}$ and inserting the result into (19) gives $n_{\mathrm{p}}\omega_{\mathrm{m}}\left[L_{\mathrm{s}}(i_{\mathrm{s}}^d)^2 + L_{\mathrm{s}}(i_{\mathrm{s}}^q)^2 + \hat{\psi}_{\mathrm{pm}}\, i_{\mathrm{s}}^d\right] = \left[R_{\mathrm{s}}(i_{\mathrm{s}}^d)^2 + R_{\mathrm{s}}(i_{\mathrm{s}}^q)^2 + n_{\mathrm{p}}\omega_{\mathrm{m}}\hat{\psi}_{\mathrm{pm}}\, i_{\mathrm{s}}^q\right]\tan(\varphi_0)$ which is a second-order polynomial in i_{s}^d. Its root with the smaller amplitude is used as d-current reference,[3] i.e.,

$$\begin{aligned} i_{\mathrm{s,ref}}^d(i_{\mathrm{s}}^q) &= -\frac{n_{\mathrm{p}}\omega_{\mathrm{m}}\hat{\psi}_{\mathrm{pm}}}{2\left(n_{\mathrm{p}}\omega_{\mathrm{m}}L_{\mathrm{s}} - R_{\mathrm{s}}\tan(\varphi_0)\right)} \\ &\quad + \sqrt{\frac{(n_{\mathrm{p}}\omega_{\mathrm{m}}\hat{\psi}_{\mathrm{pm}})^2}{4\left(n_{\mathrm{p}}\omega_{\mathrm{m}}L_{\mathrm{s}} - R_{\mathrm{s}}\tan(\varphi_0)\right)^2} - (i_{\mathrm{s}}^q)^2 + \frac{n_{\mathrm{p}}\omega_{\mathrm{m}}\hat{\psi}_{\mathrm{pm}}\, i_{\mathrm{s}}^q\tan(\varphi_0)}{\left(n_{\mathrm{p}}\omega_{\mathrm{m}}L_{\mathrm{s}} - R_{\mathrm{s}}\tan(\varphi_0)\right)}} \\ &\overset{[R_{\mathrm{s}}\approx 0]}{=} -\frac{\hat{\psi}_{\mathrm{pm}}}{2\,L_{\mathrm{s}}} + \sqrt{\left(\frac{\hat{\psi}_{\mathrm{pm}}}{2\,L_{\mathrm{s}}}\right)^2 - (i_{\mathrm{s}}^q)^2 + \frac{\hat{\psi}_{\mathrm{pm}}}{L_{\mathrm{s}}}\, i_{\mathrm{s}}^q\tan(\varphi_0)}. \end{aligned} \tag{21}$$

Hence, for large machines with $R_{\mathrm{s}} \approx 0$, the reference current $i_{\mathrm{s,ref}}^d$ depends on the machine parameters L_{s} and $\hat{\psi}_{\mathrm{pm}}$, the current i_{s}^q (or its reference $i_{\mathrm{s,ref}}^q$), and the desired phase angle φ_0. There exists an optimal value for φ_0 to minimize the THD of the phase current i_{s}^a. For the considered machine, the optimal value $\boxed{\varphi_{0,\mathrm{opt}} = \varphi_0 = 197^\circ}$ was found by iterative simulations: These results are depicted in Fig. 9(a). Clearly, for other machines, the optimal value might be different.

Finally, in Fig. 10(d), the simulation results for the overall fault-tolerant control system with extended AW, modified SVM (flat-top modulation), *and* optimally injected d-current are shown. The upper subplot depicts the currents i_{s}^d and i_{s}^q and their reference values, whereas the lower subplot illustrates the shape of the abc-currents. The THD value for this scenario is $\mathrm{THD}_{i_{\mathrm{s}}^a} = 9.4\,\%$, which is clearly the lowest compared to the other simulation results in Fig. 10(a)–(c). Moreover, the reference tracking capability, in particular, of i_{s}^q is the best, which implies that the torque ripples[4] are also minimized [recall (6)] leading to less stress on the mechanical drive train. In Fig. 9(b), the tracking of the optimal phase angle $\varphi_{0,\mathrm{opt}} = 197^\circ$ by the

[3]The solution with $-$ in front of the root would lead to a higher current magnitude.

[4]Note that if the produced generator torque in wind turbine systems does not equal its reference value, wind turbine efficiency and power production are reduced [30].

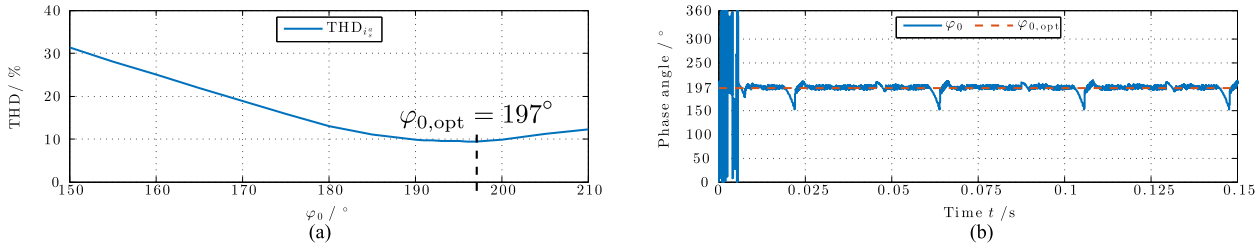

Fig. 9. Simulation results and $\mathrm{THD}_{i_\mathrm{s}^a}$ of phase current i_s^a for different phase angles $\varphi_0 \in [150°, 210°]$ and tracking of optimal phase angle $\varphi_{0,\mathrm{opt}} = 197°$ under open-switch fault in S_1 (phase a). (a) $\mathrm{THD}_{i_\mathrm{s}^a}$ for different phase angles φ_0. (b) Tracking of optimal phase angle $\varphi_{0,\mathrm{opt}} = 197°$ by actual phase angle φ_0.

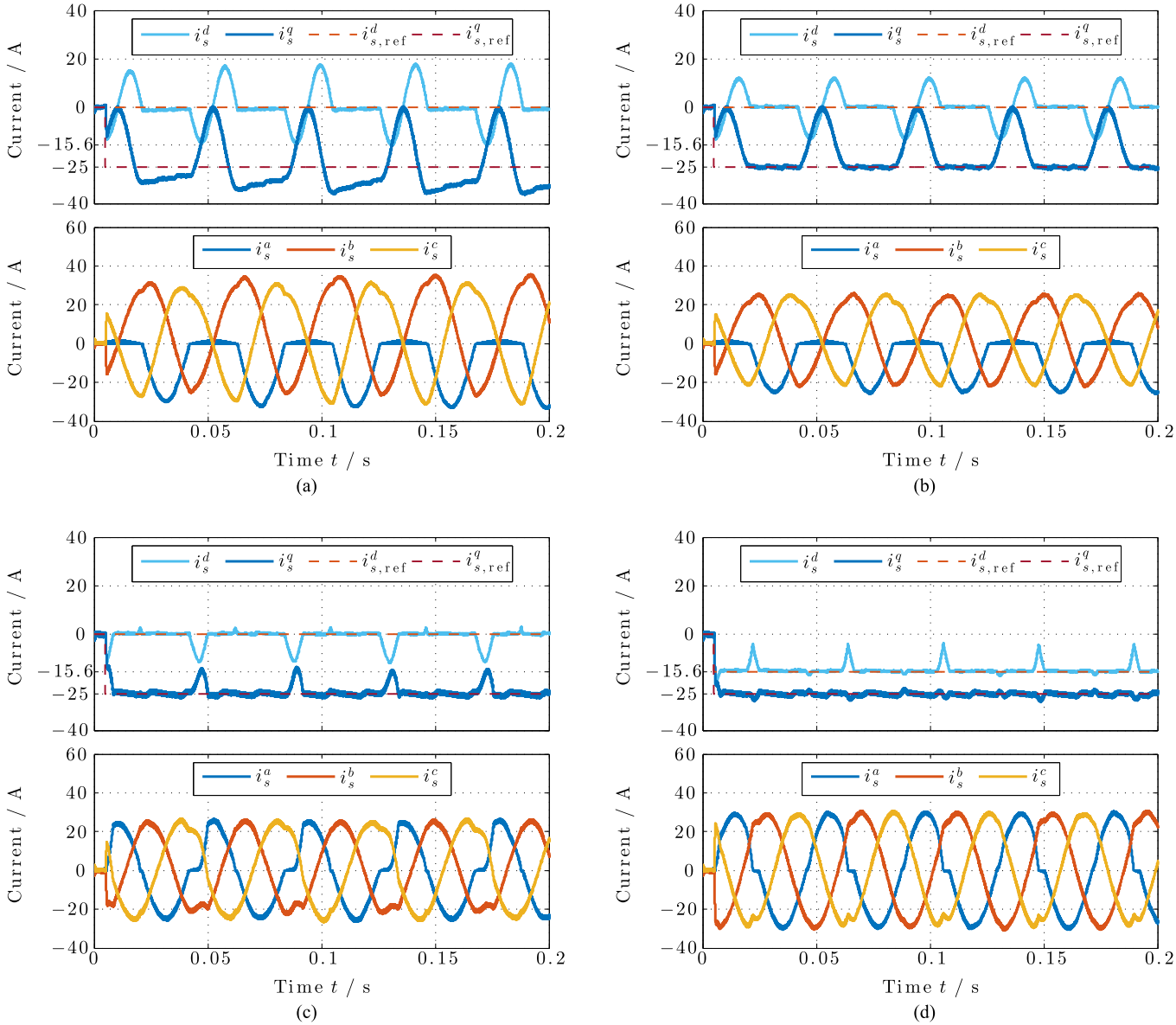

Fig. 10. Simulation results for comparative control system performance under open-switch fault in S_1 (phase a). (a) Standard control performance: $\mathrm{THD}_{i_\mathrm{s}^a} = 41.8\,\%$. (b) Improved control performance (in particular for i_s^q) due to extended AW (18): $\mathrm{THD}_{i_\mathrm{s}^a} = 41.4\,\%$. (c) Improved control performance due to extended AW (18) and modified SVM (flat-top modulation): $\mathrm{THD}_{i_\mathrm{s}^a} = 19.5\,\%$. (d) Improved control performance due to extended AW (18), modified SVM (flat-top modulation), and d-current injection: $\mathrm{THD}_{i_\mathrm{s}^a} = 9.4\,\%$.

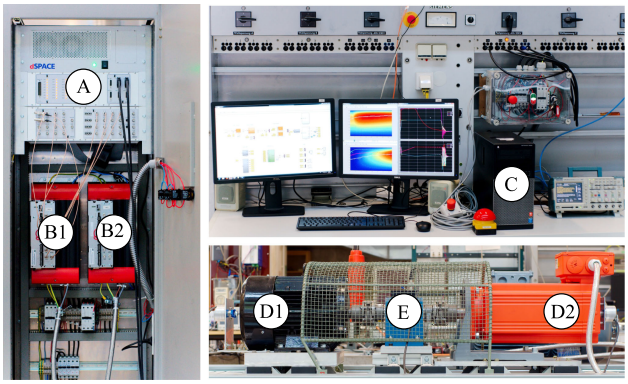

Fig. 11. Laboratory test bench with dSPACE real-time system (A), voltage-source inverters (B1) and (B2) connected back to back, host-PC (C), reluctance synchronous machine (RSM) (D1) and permanent-magnet synchronous machine (PMSM) (D2), and torque sensor (E).

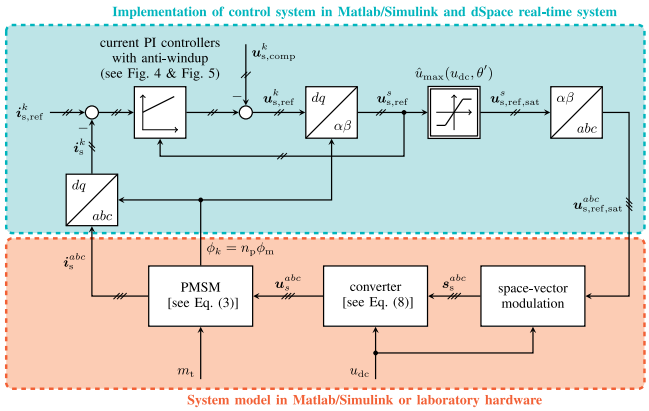

Fig. 12. Block diagram of the implementation of SVM, converter with open-switch fault in S_1, PMSG and current control system in MATLAB/Simulink and on the dSPACE real-time system.

actual phase angle φ_0 is shown. Due to the remaining time periods, where the correct voltage vector cannot be applied and the phase current is close to zero, the optimal phase angle cannot be achieved for all time.

Remark III.3 (Possible limitation of the d-current injection in wind turbine systems): Due to the current rating/limitation of the machine-side converter, the additional injection of a d-current might not be feasible up to the rated torque of the isotropic generator in wind turbine systems. Only current vector magnitudes smaller than a maximum value $\hat{i}_{\max} \geq \sqrt{(i_\mathrm{s}^d)^2 + (i_\mathrm{s}^q)^2}$ (in A) are admissible. Hence, not all currents i_s^q can be realized to obtain a desired machine torque $m_\mathrm{m} \sim i_\mathrm{s}^q$ [recall (6)]. Therefore, the uninterrupted operation of the wind turbine system under open-switch faults might not be possible for all wind speeds unless the pitch control system is incorporated into the fault-tolerant control system. The turbine torque (proportional to the wind speed and the pitch angle) must be decreased by changing the pitch angle such that the current rating of the machine-side converter is not exceeded (for details see [26] and [31, Ch. 8]).

Remark III.4 (Validity of results for faults in other switches): Since the voltage hexagon is symmetric, the optimal phase angle $\varphi_0 = 197°$ (for this particular machine) is identical for an open-switch fault in any other switch. For a fault in, e.g., S_2 and $i_\mathrm{s}^b > 0$ A, only voltage vectors within the sectors V and VI are feasible (instead of sectors III and IV for a fault in S_1). Therefore, the feasible sectors are obtained by a simple rotation by 120° [see Fig. 7]. Concluding, all conclusions made for S_1 do also hold for open-switch faults in the other switches simply by considering the respective (rotated) feasible sectors.

IV. Implementation and Experimental Verification

In this section, implementation, experimental validation, and comparison of simulation and measurement results are discussed. Three laboratory *experiments* are conducted to state the following:

(E_1) validate the accuracy of the proposed model (8) of the converter with open-switch fault (in S_1) against a real electrical drive system with open-switch fault;

TABLE II
Simulation and Measurement Data

Description	Symbol	Value and unit
Simulation parameters		
ODE-Solver		Runge-Kutta (ode4)
sampling time	h	1 µs
Converter		
DC-link voltage	u_dc	565 V
switching frequency	f_sw	8 kHz
Permanent-magnet synchronous machine (generator, isotropic)		
stator resistance	R_s	0.11 Ω
stator inductance	L_s	3.35 mH
PM-flux linkage	$\hat{\psi}_\mathrm{pm}$	0.377 V s
pole pair number	n_p	3
machine inertia	Θ_PMSG	$163 \cdot 10^{-4}$ kg m^2
Reluctance synchronous machine (anisotropic)		
stator resistance	R_s	0.4 Ω
stator inductances	$L_\mathrm{s}^d \neq L_\mathrm{s}^q$	nonlinear (see [33, Fig. 2])
pole pair number	n_p	2
machine inertia	Θ_RSM	$189 \cdot 10^{-4}$ kg m^2
Current control system of PMSG		
PI controller gains	$k_\mathrm{p}^d = k_\mathrm{p}^q$	8.93 $\frac{\mathrm{V}}{\mathrm{A}}$
	$k_\mathrm{i}^d = k_\mathrm{i}^q$	293.3 $\frac{\mathrm{V}}{\mathrm{A\,s}}$
max. AW current	$\hat{i}_\mathrm{aw}$	−1 A

(E_2) verify the effectiveness of the proposed modifications (such as extension of the AW strategy, flat-top modulation, and injection of an optimal d-current) on the generator control performance and to compare simulation and experimental results;

(E_3) illustrate the impact of an occurring open-switch fault (after a fault-free interval) and then, step-by-step, the positive effect of each proposed modification on the control performance of the laboratory system.

A. Experimental Setup and Implementation

The measurements were conducted on a 10-kW laboratory test bench, as depicted in Fig. 11. The anisotropic *RSM* is speed controlled (with underlying nonlinear current controllers [32]). The isotropic *PMSM* is used as generator and current controlled

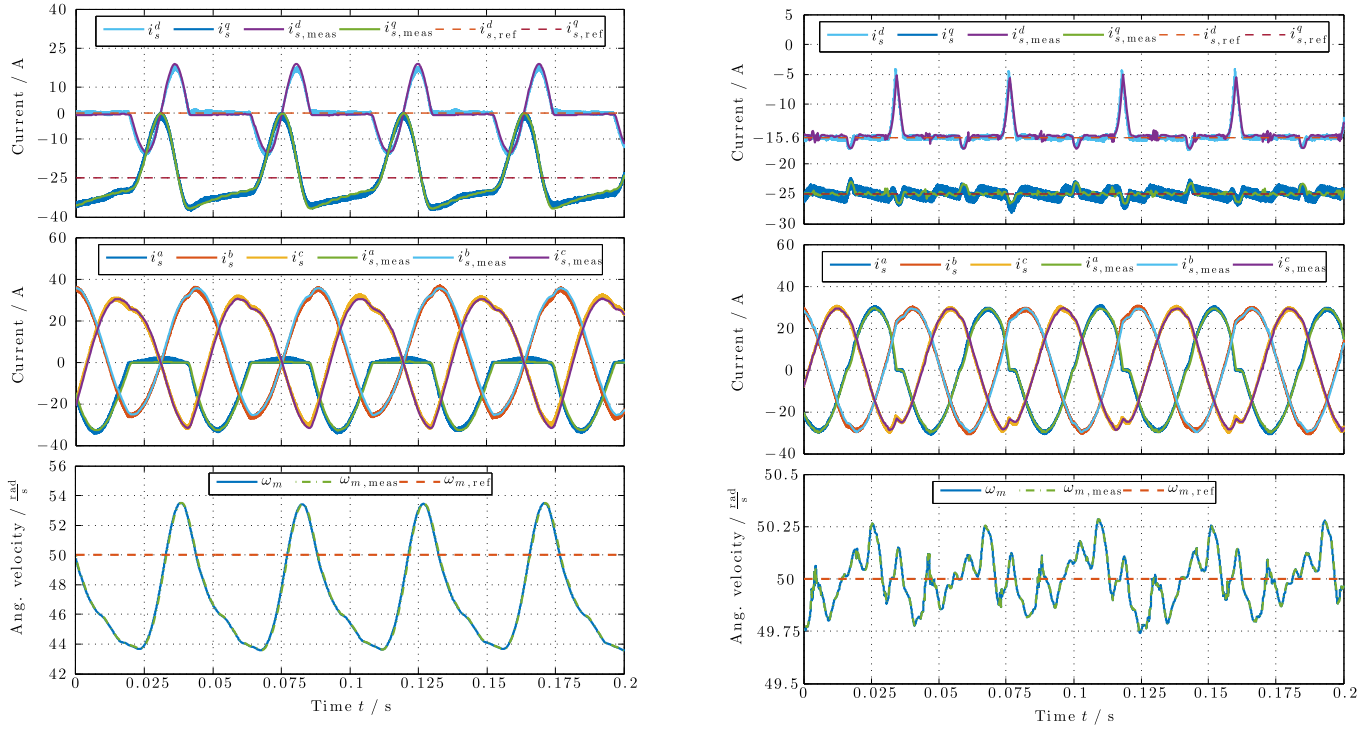

Fig. 13. Comparison of simulation and measurement results for standard control system and fault-tolerant control system with extended AW, modified SVM (flat-top modulation), and optimally injected d-current. (a) Experiment (E_1): Comparison of simulation and measurement results for standard control system: $\mathrm{THD}_{i_s^a} = 41.8\,\%$ (simulation) versus $\mathrm{THD}_{i_s^a,\mathrm{meas}} = 45.4\,\%$ (measurement). (b) Experiment (E_2): Comparison of simulation and measurement results for fault-tolerant control system: $\mathrm{THD}_{i_s^a} = 9.4\,\%$ (simulation) versus $\mathrm{THD}_{i_s^a,\mathrm{meas}} = 10.6\,\%$ (measurement).

as described in the previous sections. Both drives are controlled by a dSPACE real-time system, which applies the switching signals (switching vectors) to the respective inverter/converter. Both converters are connected back to back. The PMSG converter is modified such that each upper and lower switch can be addressed individually and allows to emulate open-switch faults. For all experiments, without loss of generality, open-switch faults in S_1 (phase a) were considered, simulated, and emulated.

The implementation for simulations and measurements was performed using MATLAB/Simulink. In Fig. 12, the block diagram of the implementation is shown. The parameters of the laboratory setup are listed in Table II (where $\Theta = \Theta_{\mathrm{RSM}} + \Theta_{\mathrm{PMSG}}$) and coincide with those used for the simulations. Note that the measured currents were filtered (by an analog filter in the converter) and, then, sampled with the switching frequency, whereas the simulated currents were *not* filtered.

B. Discussion of Experiments

1) Experiment (E_1): The simulation *and* measurement scenario of this experiment is as follows: The PMSG-side converter emulates an open-switch fault in S_1 and the standard control system (as described in Section III-A) was implemented. Simulation and measurement results of Experiment (E_1) are shown in Fig. 13(a). The measured quantities are labeled with the additional subscript "meas." Obviously, simulation and measurement results match very closely. Hence, the proposed mathematical model (8) is valid and allows to simulate the behavior of the real system precisely. Note that, due to the smaller power rating of the RSM, the speed controller for the RSM is not capable to compensate for the large torque/current ripples induced by the faulty PMSG converter.

2) Experiment (E_2): For this experiment, again an open-switch fault in S_1 (phase a of the PMSG) is emulated; but this time, the fault-tolerant control system (extended FOC, as proposed in Section III-B) with extended AW, flat-top modulation, and optimal i_{s}^d-injection (with $\varphi_0 = 197°$) is implemented for simulation and measurement. Fig. 13(b) shows the comparative simulation and measurement results. Again, simulation and measurement results match very closely. Moreover, also the THD values $\mathrm{THD}_{i_s^a} = 9.4\,\%$ and $\mathrm{THD}_{i_s^a,\mathrm{meas}} = 10.6\,\%$ are almost identical. In conclusion, the proposed modifications are also effective in real world and the outcomes of the theoretical and simulative analysis in Section III-B are confirmed.

3) Experiment (E_3): For the last experiment, the measurement scenario comprises a sequence of events [see Fig. 14] as follows:

1. time interval: standard control system (without open-switch fault/fault-free case);
2. time interval: standard control system under open-switch fault in S_1;

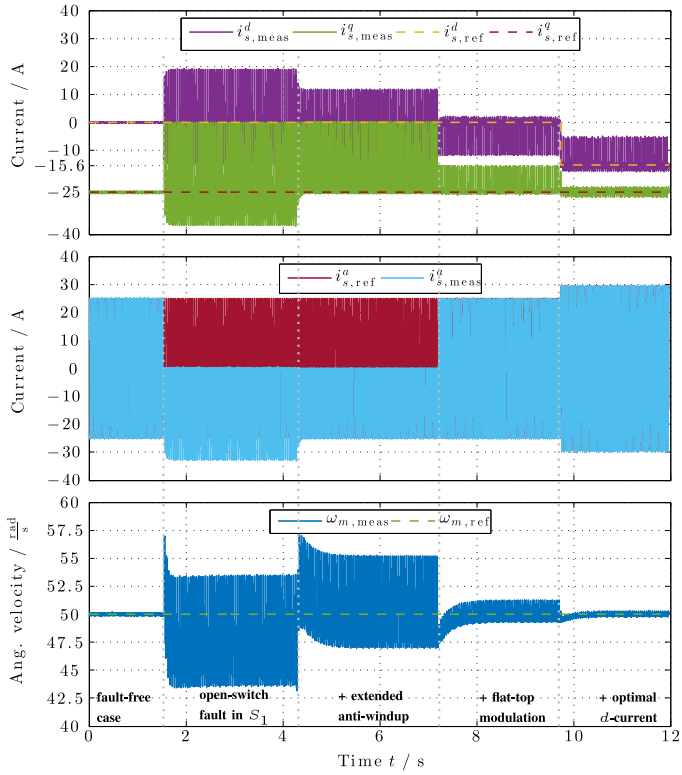

Fig. 14. Experiment (E_3): Measurement results for current control system during five different scenarios. 1) Fault-free case. 2) Open-switch fault in S_1. 3) With extended AW. 4) Additionally with flat-top modulation. 5) Additionally with optimal d-current injection.

3. time interval: standard control system with extended AW under open-switch fault in S_1;
4. time interval: standard control system with extended AW *and* flat-top modulation under open-switch fault in S_1;
5. time interval: fault-tolerant control system with extended AW, flat-top modulation, *and* optimal d-current injection under open-switch fault in S_1.

V. Conclusion

In this paper, a generic mathematical model of a two-level converter with open-switch faults has been derived. The output voltages of the faulty converter can be computed based on switching vector, dc-link voltage, and sign of the current in the phase with the open-switch fault. The model holds for faults in each of the six switches. In the next step, the impact of an open-switch fault on the current control system of isotropic PMSGs has been investigated. If the faulty switch is known and the corresponding diode is still working properly, three easy-to-implement extensions to the control system have been proposed to improve fault tolerance and control performance under faults. The three modifications reduce the THD of the faulty phase current, the torque ripples and, therefore, the stress on the mechanical drive train. Moreover, a safe and uninterrupted operation of the generator can be guaranteed. The proposed modifications are as follows:

1) extension of the AW strategy in the current PI controllers;
2) modification of the SVM (flat-top modulation);
3) injection of optimal d-currents.

All modifications have been explicitly illustrated and implemented for an open-switch fault in phase a; however, the generic model and the provided descriptions allow to implement the modifications for any other open-switch fault in the converter. Finally, comparative simulation and measurement results illustrate and validate 1) the accuracy of the proposed model of the faulty converter and 2) the effectiveness and functionality of the proposed modifications on a laboratory test bench.

Acknowledgment

The authors are deeply indebted to M. Lindner for adapting the laboratory test bench to make measurements of a converter with open-switch faults possible.

References

[1] K. Rothenhagen and F. W. Fuchs, "Performance of diagnosis methods for IGBT open circuit faults in three phase voltage source inverters for AC variable speed drives," in *Proc. Eur. Conf. Power Electron. Appl.*, Sep. 2005, pp. 1–10.
[2] H. Zhao and L. Cheng, "Open-switch fault-diagnostic method for back-to-back converters of a doubly fed wind power generation system," *IEEE Trans. Power Electron.*, vol. 33, no. 4, pp. 3452–3461, Apr. 2018.
[3] B. Lu and S. K. Sharma, "A literature review of IGBT fault diagnostic and protection methods for power inverters," *IEEE Trans. Ind. Appl.*, vol. 45, no. 5, pp. 1770–1777, Sep. 2009.
[4] U. M. Choi, J. S. Lee, F. Blaabjerg, and K. B. Lee, "Open-circuit fault diagnosis and fault-tolerant control for a grid-connected NPC inverter," *IEEE Trans. Power Electron.*, vol. 31, no. 10, pp. 7234–7247, Oct. 2016.
[5] J. S. Lee, K. B. Lee, and F. Blaabjerg, "Open-switch fault detection method of a back-to-back converter using NPC topology for wind turbine systems," *IEEE Trans. Ind. Appl.*, vol. 51, no. 1, pp. 325–335, Jan. 2015.
[6] U. M. Choi, K. B. Lee, and F. Blaabjerg, "Diagnosis and tolerant strategy of an open-switch fault for T-type three-level inverter systems," *IEEE Trans. Ind. Appl.*, vol. 50, no. 1, pp. 495–508, Jan. 2014.
[7] U. M. Choi, H. G. Jeong, K. B. Lee, and F. Blaabjerg, "Method for detecting an open-switch fault in a grid-connected NPC inverter system," *IEEE Trans. Power Electron.*, vol. 27, no. 6, pp. 2726–2739, Jun. 2012.
[8] W.-S. Im, J.-S. Kim, J.-M. Kim, D.-C. Lee, and K.-B. Lee, "Diagnosis methods for IGBT open switch fault applied to 3-phase AC/DC PWM converter," *J. Power Electron.*, vol. 12, no. 1, pp. 120–127, 2012.
[9] N. M. A. Freire, J. O. Estima, and A. J. M. Cardoso, "Open-circuit fault diagnosis in PMSG drives for wind turbine applications," *IEEE Trans. Ind. Electron.*, vol. 60, no. 9, pp. 3957–3967, Sep. 2013.
[10] H. T. Eickhoff, R. Seebacher, A. Muetze, and E. Strangas, "Enhanced and fast detection of open switch faults in inverters for electric drives," *IEEE Trans. Ind. Appl.*, vol. 53, no. 6, pp. 5415–5425, Nov./Dec. 2017.
[11] R. L. de Araujo Ribeiro, C. B. Jacobina, E. R. C. da Silva, and A. M. N. Lima, "Fault detection of open-switch damage in voltage-fed PWM motor drive systems," *IEEE Trans. Power Electron.*, vol. 18, no. 2, pp. 587–593, Mar. 2003.
[12] K. H. Kim, D. U. Choi, B. G. Gu, and I. S. Jung, "Fault model and performance evaluation of an inverter-fed permanent magnet synchronous motor under winding shorted turn and inverter switch open," *IET Elect. Power Appl.*, vol. 4, no. 4, pp. 214–225, Apr. 2010.
[13] S. M. Jung, J. S. Park, H. W. Kim, K. Y. Cho, and M. J. Youn, "An MRAS-based diagnosis of open-circuit fault in PWM voltage-source inverters for PM synchronous motor drive systems," *IEEE Trans. Power Electron.*, vol. 28, no. 5, pp. 2514–2526, May 2013.
[14] W. S. Im, J. M. Kim, D. C. Lee, and K. B. Lee, "Diagnosis and fault-tolerant control of three-phase AC-DC PWM converter systems," *IEEE Trans. Ind. Appl.*, vol. 49, no. 4, pp. 1539–1547, Jul. 2013.
[15] P. Sobanski and T. Orlowska-Kowalska, "Analysis of space vector modulation technique in inverter-fed fault-tolerant induction motor drive," in *Proc. 16th Int. Power Electron. Motion Control Conf. Expo.*, Sep. 2014, pp. 1024–1029.
[16] W. S. Im, J. J. Moon, J. M. Kim, D. C. Lee, and K. B. Lee, "Fault tolerant control strategy of 3-phase AC-DC PWM converter under multiple open-switch faults conditions," in *Proc. 27th Annu. IEEE Appl. Power Electron. Conf. Expo.*, Feb. 2012, pp. 789–795.

[17] S. M. Jung, K. Lee, and H. W. Kim, "Post-fault operation of open-circuit fault in three-phase PWM converter," in *Proc. 16th Int. Power Electron. Motion Control Conf. Expo.*, Sep. 2014, pp. 311–316.
[18] J. S. Lee and K. B. Lee, "An open-switch fault detection method and tolerance controls based on SVM in a grid-connected T-type rectifier with unity power factor," *IEEE Trans. Ind. Electron.*, vol. 61, no. 12, pp. 7092–7104, Dec. 2014.
[19] J. S. Lee and K. B. Lee, "Open-switch fault tolerance control for a three-level NPC/T-type rectifier in wind turbine systems," *IEEE Trans. Ind. Electron.*, vol. 62, no. 2, pp. 1012–1021, Feb. 2015.
[20] N. M. A. Freire, "Fault-tolerant permanent magnet synchronous generator drives for wind turbine applications," Ph.D. dissertation, Electr. Comput. Eng. Dept. Faculty Sci. Tech., Univ. Coimbra, Coimbra, Portugal, 2013.
[21] A. Gaeta, G. Scelba, and A. Consoli, "Modeling and control of three-phase PMSMs under open-phase fault," *IEEE Trans. Ind. Appl.*, vol. 49, no. 1, pp. 74–83, Jan. 2013.
[22] O. Wallmark, L. Harnefors, and O. Carlson, "Post-fault operation of fault-tolerant inverters for PMSM drives," in *Proc. Eur. Conf. Power Electron. Appl.*, Sep. 2005, pp. 1–10.
[23] S. Bolognani, M. Zordan, and M. Zigliotto, "Experimental fault-tolerant control of a PMSM drive," *IEEE Trans. Ind. Electron.*, vol. 47, no. 5, pp. 1134–1141, Oct. 2000.
[24] C. M. Hackl, *Non-Identifier Based Adaptive Control in Mechatronics: Theory and Application* (Lecture Notes in Control and Information Sciences), vol. 466. Berlin, Germany: Springer, 2017. [Online]. Available: http://www.springer.com/de/book/9783319550343
[25] R. De Doncker, D. W. Pulle, and A. Veltman, *Advanced Electrical Drives* (Power Systems). Berlin, Germany: Springer-Verlag, 2011.
[26] C. Dirscherl, C. Hackl, and K. Schechner, "Modellierung und Regelung von modernen Windkraftanlagen: Eine Einführung," in *Elektrische Antriebe – Regelung von Antriebssystemen*, D. Schröder, Ed. New York, NY, USA: Springer-Verlag, 2015, ch. 24, pp. 1540–1614 (see https://arxiv.org/abs/1703.08661 for the English translation).
[27] D. Schröder, *Elektrische Antriebe - Regelung von Antriebssystemen*, 4th ed. Berlin, Germany: Springer-Verlag, 2015.
[28] D. Shmilovitz, "On the definition of total harmonic distortion and its effect on measurement interpretation," *IEEE Trans. Power Del.*, vol. 20, no. 1, pp. 526–528, Jan. 2005.
[29] R. Valentine, *Motor Control Electronics Handbook* (McGraw-Hill Handbooks). New York, NY, USA: McGraw-Hill, 1998.
[30] C. Hackl and K. Schechner, "Non-ideal feedforward torque control of wind turbines: Impacts on annual energy production & gross earnings," *J. Phys., Conf. Ser.*, vol. 753, no. 11, 2016, Art. no. 112010. [Online]. Available: http://stacks.iop.org/1742-6596/753/i=11/a=112010
[31] T. Burton, D. Sharpe, N. Jenkins, and E. Bossanyi, *Wind Energy Handbook*, 2nd ed. Hoboken, NJ, USA: Wiley, 2011.
[32] C. M. Hackl, M. J. Kamper, J. Kullick, and J. Mitchell, "Current control of reluctance synchronous machines with online adjustment of the controller parameters," in *Proc. IEEE Int. Symp. Ind. Electron.*, Santa Clara, CA, USA, Jun. 2016, pp. 153–160.
[33] H. Eldeeb, C. M. Hackl, L. Horlbeck, and J. Kullick, "Analytical solutions for the optimal reference currents for MTPC/MTPA, MTPV and MTPF control of anisotropic synchronous machines," in *Proc. IEEE Int. Elect. Mach. Drives Conf.*, Miami, FL, USA, 2017, pp. 1–6.

Christoph M. Hackl (M'12–SM'16) was born in Mannheim, Germany, in 1977. He studied electrical engineering (controls and mechatronics) at the Technical University of Munich (TUM), Munich, Germany, and the University of Wisconsin-Madison, Madison, WI, USA. He received the B.Sc., Dipl.Ing., and Dr. Ing. (Ph.D.) degrees from the TUM, in 2003, 2004, and 2012, respectively.

Since 2004, he has been teaching electrical drives, power electronics, and mechatronic and renewable energy systems. Since 2014, he has been heading the "Control of Renewable Energy Systems" Research Group, TUM. In 2018, he was appointed Professor for electrical machines and drives with the Munich University of Applied Sciences, Munich, Germany. His research interests include nonlinear, adaptive, and optimal control of electric, mechatronic, and renewable energy systems.

Urs Pecha studied renewable energy engineering and electrical engineering at the University of Stuttgart, Stuttgart, Germany, Chalmers University of Technology, Göteborg, Sweden, and the Technical University of Munich, Munich, Germany. He received the B.Sc. and M.Sc. degrees in 2014 and 2017, respectively. Since 2017, he has been working toward the Dr. Ing. (Ph.D.) degree at the Institute of Electrical Energy Conversion, University of Stuttgart.

His research interests include optimal control of renewable energy systems and increased reliability of electric drive systems.

Korbinian Schechner studied "electrical engineering and information technology" with focus on power engineering, electrical drives and control at the Technical University of Munich (TUM), Munich, Germany, where he received the B.Sc. and M.Sc. degrees in 2011 and 2013, respectively.

Since 2014, he has been with the "Control of Renewable Energy Systems" Research Group, Munich School of Engineering, TUM. His research interests include modeling and control of renewable energy systems with a special focus on fault detection and postfault control strategies.